# Pore-scale imaging of hydrogen displacement and trapping in porous media

*Eike M. Thaysen*[1*], *Ian B. Butler*[1], *Aliakbar Hassanpouryouzband*[1], *Damien Freitas*[1], *Fernando Alvarez-Borges*[2], *Samuel C. Krevor*[3], *Niklas Heinemann*[1], *Robert Atwood*[2], *Katriona Edlmann*[1]

[1]School of Geoscience, Grant Institute, The King's Buildings, The University of Edinburgh, James Hutton Road, Edinburgh, EH9 3FE, United Kingdom

[2] Diamond Light Source Ltd, Harwell Campus, Didcot OX11 0DE, United Kingdom

[3] Department of Earth Science and Engineering, Imperial College London, London SW7 2AZ, United Kingdom

[*] = corresponding author email, phone number: eike.thaysen@ed.ac.uk, +34 682079236

**Abstract**

Hydrogen can act as an energy store to balance supply and demand in the renewable energy sector. Hydrogen storage in subsurface porous media could deliver high storage capacities but the volume of recoverable hydrogen is unknown. We imaged the displacement and capillary trapping of hydrogen by brine in a Clashach sandstone cylinder at 2-7 MPa pore fluid pressure using X-ray computed microtomography. Hydrogen saturation obtained during drainage at capillary numbers of $<10^{-7}$ was ~50% of the pore volume and independent of the injection pressure. Fluid configuration in the pore space was indicative of a water wetting system at all conditions. Capillary trapping of hydrogen via snap-off during secondary imbibition at a capillary number of $2.4x10^{-6}$ systematically increased with pressure, 20%, 24% and 43% of the initial hydrogen trapped at 2, 5 and 7 MPa, respectively. Injection of brine at increasing capillary numbers up to $9.4x10^{-6}$ reduced capillary trapping. Based on these results, we recommend more shallow, lower pressure sites for future hydrogen storage operations in porous media.

Keywords: geological hydrogen storage, μCT, porous media, recovery, drainage, imbibition

Highlights:

- Hydrogen injectivity and recovery in rock is imaged with x-ray computed micro-CT
- Hydrogen recovery decreases with increasing reservoir depth
- Hydrogen recovery increases with increasing brine flow rate
- Hydrogen trapping occurs via snap-off processes
- Nitrogen is a poor proxy for hydrogen

## 1. Introduction

The storage of surplus electrical energy could increase the utility of renewable energy sources thereby reducing the environmental impact of energy generation[1, 2]. Storage mediums like batteries, compressed air, capacitors, or flywheels are only applicable for the short-term and small-scale electricity storage[3]. The use of hydrogen ($H_2$) as an energy vector however could provide long-term storage to balance the intermittent demand and supply challenges affecting renewable methods[3]. Considering the low energy density of $H_2$[4], storage of $H_2$ in large storage sites is the only solution for economical, gigawatt to terawatt-scale $H_2$ storage. Underground storage of $H_2$ in salt caverns is an established technology[5], yet, only subsurface porous media (saline aquifers and depleted oil and gas fields), can provide TWh storage capacities that could balance seasonal demands[4]. Relative to cavern storage, inter-seasonal storage in porous media is poorly understood and introduces a range of other complexities[2], including potential pore-clogging by microbial growth[6], gas loss out of diffuse lateral boundaries, viscous fingering of $H_2$ into reservoir brines, residual trapping and possible reactions with the primary formation fluid and reservoir minerals[7-10]. Each of these requires consideration of multiphase flow, transport and reaction[2, 8].

Recent years have seen several studies on $H_2$ geochemistry[11-13] and the elucidation of many important flow characteristics of $H_2$ including; Hydrogen relative permeability[14, 15], interfacial tension (IFT)[16, 17], and $H_2$/brine/rock contact angles[14, 16-24]. Yet, additional data describing the $H_2$ fluid flow in different porous formations and under varying conditions are vital to make accurate predictions of the $H_2$ plume development and to define optimum production strategies[8]. Of particular relevance is the degree of capillary trapping, which leads to a reduced volume of recoverable $H_2$, in this way impacting the economic feasibility of the operation[8]. The capillary forces that control capillary trapping also control the relative permeability[8]. As such

studies on residual trapping give insight to a range of crucial input parameters for pore-scale and reservoir $H_2$ storage models.

The effects of the brine pore fluid pressures and of brine flow rate on capillary trapping of $H_2$ are hithertho unknown. The brine pore fluid pressure is linked to the reservoir depth via the hydrostatic gradient, hence an investigation of the latter could facilitate the definition of an optimal storage depth for gas recovery. The flowrate affects the capillary number, $N_c$, via equation 1:

$$N_C = \frac{q \cdot \mu}{\sigma} \quad (1)$$

where $q$ is the flow, $\mu$ is the viscosity and $\sigma$ is the interfacial tension (IFT). As $N_c$ increases, viscous forces dominate capillary forces and capillary trapping of the nonwetting phase decreases[25]. This capillary desaturation with increasing $N_c$, depends on the rock type[26] and on the kind of nonwetting phase[25] and is observed around critical capillary numbers of $10^{-5}$ to $10^{-8}$ [25].

A non-destructive standard technique for visualization and analysis of wetting and non-wetting phase displacement processes in porous media is x-ray micro-computed tomography (µCT)[27]. Pore-scale models are directly reliant on µCT images to build up the basic models for appropriate understanding of gas storage operations[28]. Previously published µCT studies on two-phase flow in porous media involving gas have largely focused on supercritical carbon dioxide ($sCO_2$) in sandstones and limestones, e.g.[27, 29-34]. Reported saturations of $sCO_2$ in non-aged (i.e. not wettability altered by exposure to oil or organic acids) water-wet rocks range from 30-60% during drainage and 15-30% during imbibition, at $N_{Ca}$ between $10^{-8}$ to $10^{-6}$ and $10^{-8}$ to $2x10^{-5}$, respectively[27, 30, 32-34]. Studies using subcritical, gaseous carbon dioxide ($CO_2$), which could be more readily compared to $H_2$, are scarce. Yet, the characteristic trapping curves for $sCO_2$ and $CO_2$, which show the residual saturation ($S_{nnwr}$) as a function of initial saturation ($S_{nwi}$), are not significantly different[35]. Saturations of nitrogen ($N_2$) during drainage and

91 imbibition in sandstones with 6-22% porosity is 43-64% and 43%, respectively, at $N_C$ between
92 1-7x10$^{-8}$ [36, 37]. Carbon dioxide trapping increases at lower pressures due to decreasing water
93 contact angles[38]. Unlike in $CO_2$ storage, trapping is not desirable in geological $H_2$ storage as it
94 leads to unrecoverable $H_2$.
95 Some observational studies have suggested that $H_2$ is less wetting on rocks than $CO_2$[19, 21]. At
96 the time of writing two μCT studies, one micro-model study and one nuclear magnetic
97 resonance (NMR) study on $H_2$ exist: Al-Yaseri et al. (2022)[39] used NMR to find $H_2$ $S_{nwi}$ and
98 $S_{nwr}$ of 4% and <2%, respectively, in a Fontainebleau sandstone at 0.4 MPa and ambient
99 temperature. Higgs et al. (2021)[16] μCT-imaged $H_2$ injection into a 5 mm diameter and 7.6 mm
100 length core of Bentheimer sandstone at pressures of 6.8 to 20.8 MPa and documented
101 decreasing IFT between $H_2$ and water with increasing pressure (72.5 mN/m at 6.9 MPa to 69.4
102 mN/m at 20.7 MPa). Jha et al. (2021)[40] conducted a single cycle $H_2$-brine displacement
103 sequence in a 5 mm diameter and 15 mm length Gosford sandstone, and used μCT to calculate
104 an $S_{nwi}$ of 65% during drainage and a $S_{nnwr}$ of 41% after brine imbibition. Rock samples in Jha
105 et al. (2021)[40] and Higgs et al. (2021)[16] were sufficiently short for capillary end effects to
106 dominate the flow behaviour, where the wetting phase accumulates close to the production face
107 of the core[41]. The experiment by Jha et al. (2021)[40] was performed at ambient pressure and
108 leaves open the question of variations in $H_2$ wetting and flow behaviour at reservoir
109 conditions[19]. Increasing pore fluid pressures have been reported to increase the gas saturation
110 and pore network connectivity for nitrogen ($N_2$) in a brine wet, aged Bashijiqike tight sandstone
111 (0.6% gas saturation at 2 MPa versus 43% at 8 MPa)[36]. The effect of $N_C$ increases from 7.7x10$^{-7}$
112 to 3.8x10$^{-4}$ on the $H_2$ flow through a sandstone micro-model at 0.5 MPa was investigated by
113 Lysyy et al. (2022)[20] who found that $H_2$ saturation increased correspondingly from 18% to
114 79%[20].

115 In this work, we used μCT to investigate the displacement and capillary trapping of $H_2$ by brine
116 in 4.7 mm diameter and 54-57 mm length Clashach sandstone cores as a function of gas and
117 brine pore fluid pressure (2-7 MPa) and flow rate (20 to 80 μl $min^{-1}$, corresponding to $H_2$ and
118 brine bulk $N_C$ of 1.7-6.8x$10^{-8}$ and 1.2-9.4x$10^{-6}$, respectively). We show that the $H_2$ $S_{nwi}$ is
119 independent of pore fluid pressure but that higher brine pore fluid pressures during secondary
120 imbibition increase capillary trapping of $H_2$, indicating increased trapping at elevated reservoir
121 depths. Higher flowrates during secondary imbibition on the other hand decrease capillary
122 trapping. Our work advances the current understanding of $H_2$ flow in porous media by
123 delivering the first realistic estimates on how much $H_2$ can be recovered from the subsurface
124 after injection, disregarding any $H_2$ loss by microbial or geochemical reactions, as a function
125 of reservoir depth and flow rate.
126

127 **2. Materials and Methods**

128 *2.1 Core-flooding experiments*

129 We performed non-steady and steady state, two-phase core flooding experiments with $H_2$
130 (purity 99.9995 vol.%, BOC Ltd.) and brine (0.5 M CsCl or 2 M KI, Sigma-Aldrich) in a
131 Clashash sandstone (Permian, Aeolian sandstone from near Elgin in Scotland. Clashach
132 composition: ~96 wt.% quartz, 2% K-feldspar, 1% calcite, 1% ankerite[42], porosity 11.1-
133 14.4%[42-44]) at ambient temperature (~293 K). The Clashach sandstone, with its low
134 mineralogical variability, yet still comparably big pore space, was chosen in order to facilitate
135 the visualization of the injected $H_2$ and the interpretation of the results.
136 Two types of experiments were carried out: The first set of experiments (from now on referred
137 to as UoE (Univeristy of Edinburgh) experiments) was carried out using the μCT instrument
138 at the University of Edinburgh and were aimed at imaging the displacement and capillary

139 trapping of $H_2$ by brine as a function of saturation after drainage and imbibition under different
140 experimental conditions. Three UoE experiments were carried out that investigated the effect
141 of injection pressure (2-7 MPa), whereof each was repeated once (UoE exp. 1-3, Table 1). The
142 standard error on the $H_2$ saturation in the repeated experiments was calculated as the standard
143 deviation devided by the square root of the number of repeated experiments. One UoE
144 experiment looked at the effect of the $H_2$/brine injection ratio on the $H_2$ saturation (UoE exp.
145 4, Table 1). This experiment was carried out to evaluate the effect of $H_2$ injection into aquifers
146 with different magnitudes of brine flow (hydrodynamic aquifers), and to simulate the far field
147 situation, where $H_2$ and brine move together. Another UoE experiment investigated the effect
148 of secondary drainage and imbibition (UoE exp. 5, Table 1). UoE exp. 6 used $N_2$ instead of $H_2$.
149 This experiment was undertaken in order to compare the flow behaviour of the two gases,
150 which is of relevance because $N_2$ is sometimes used as an analogue for $H_2$, e.g. in permeability
151 measurements[11, 15]. Because rearrangement processes in the pore volume were noted previously
152 for $N_2$[36], UoE exp. 7 (Table 1) was undertaken to examine the stability of $H_2$ in the rock volume
153 over an experimental duration (10 hours): Ten PV of $H_2$ were injected into a brine-saturated
154 rock and keeping the pressure constant inside the pressure vessel, with imaging undertaken at
155 the start and after 10 hours. The effect of bulk capillary number on drainage and imbibition
156 was deduced by a comparison of the results from UoE exp. 2 and 5 which used flowrates of 20
157 and 80 µl $min^{-1}$, respectively, and 5 MPa injection pressure (Table 1).
158 The second type of experiment (from now on referred to as the 'dry rock experiment'; Table
159 1) used synchrotron radiation (Diamond Light Source, I12-JEEP tomography beamline) to
160 capture the time-resolved displacement of $H_2$ by brine in a dry, $H_2$-saturated rock. This
161 experiment served as a base of comparison to the displacements of $H_2$ in wet, brine-saturated
162 rock (UoE experiments).
163 All experiments used a bespoke x-ray transparent core holder for a 5 mm diameter rock core,

164 **Table 1: Overview over experiments**

| Experiment | Type of x-ray source | Description | Sample | $H_2$/brine injection ratio(s) | Flowrate (µl $min^{-1}$) | Injection Pressure (MPa) | Confining Pressure (MPa) | Pore volumes injected | Repetitions of experiment |
|---|---|---|---|---|---|---|---|---|---|
| UoE exp. 1 | laboratory | Primary drainage and imbibition in non-steady state displacements of $H_2$ and brine | 1 | - | 20 | 7 | 9 | 10 | 1 entire repetition, 1 repetition on drainage only |
| UoE exp. 2 | laboratory | Primary drainage and imbibition in non-steady state displacements of $H_2$ and brine | 1 | - | 20 | 5 | 9 | 10 | 1 |
| UoE exp. 3 | laboratory | Primary drainage and imbibition in non-steady state displacements of $H_2$ and brine | 1 | - | 20 | 2 | 9 | 10 | 1 |
| UoE exp. 4 | laboratory | Simultaneous, steady state injections of $H_2$ and brine | 1 | 1:4, 1:1, 4:1 | 20 | 5 | 9 | 10 | - |
| UoE exp. 5 | laboratory | Primary and secondary drainage and imbibition in non-steady state displacements of $H_2$ and brine | 1 | - | 80 | 5 | 9 | 10 | - |
| UoE exp.6 | laboratory | Non-steady state displacements of $N_2$ and brine | 1 | - | 20 | 5 | 9 | 10 | - |
| UoE exp.7 | laboratory | $H_2$ stability | 1 | - | 80 | 5 | 9 | 10 | - |
| Dry rock | synchrotron | Non-steady state, brine injection into dry, $H_2$ saturated rock | 2 | - | 5 | 5 | 10 | 10 | - |

165

which was a scaled-up version of the cell described by Fusseis et al. (2014)[45]. In UoE experiments a carbon-fibre reinforced PEEK pressure vessel was used to permit good x-ray transparency. The dry rock experiment used an aluminium pressure vessel to comply with the health and safety requirements at Diamond Light Source. The specifications of the pressure vessels of PEEK and aluminium were engineered with safety factors of 2 times or more over and above the maximum applied confining pressure (10 MPa; Table 1).

Rock cores for the experiments were obtained by diamond drill coring with a water-flushed chuck, followed by preparation of the core ends by grinding on a lathe. Experiments used a set of four high-pressure pumps (Cetoni Nemesys$^{TM}$, flowrate range 0.072 nl $s^{-1}$ to 13.76 ml $s^{-1}$): One for the injection of $H_2$, one for the injection of brine, one to hold the backpressure and one for the confining pressure (Fig. 1). A bespoke manifold system composed of high-pressure 1/8" and 1/16" 316 stainless steel and 1/16" PEEK tubing (Swagelok, Top Industrie and Cole Parmer, respectively) connected the pumps to the core-flood cell (Fig. 1). Additional pressure transducers (ESI Technology; accuracy 0.1% full-scale) were coupled to the flow system at the inlet and outlet to allow for higher precision pressure monitoring than was possible using the integral pressure gauges in the syringe pumps. Cyclic $H_2$ and brine injections used a Clashach outcrop sample without further cleaning of 4.7 mm diameter and a relatively long length of 54-57 mm to avoid the influences of capillary end effects[46, 47]. To prevent leakage of $H_2$ into the confining fluid, the rocks were jacketed in aluminium foil and poluolefin heatshrink tubing and sealed with silicone adhesive between the conical-ended pistons within the pressure vessel. In UoE experiments, a water-wet rock was first saturated with brine (0.5 M CsCl) at a flow rate of 70 µl $min^{-1}$. Afterwards, $H_2$ was injected (drainage) into the brine-saturated rock at flow rates of 20-80 µl $min^{-1}$, based on desired capillary-regime $N_C$ of 1.7-6.8x$10^{-8}$ (The viscosity of $H_2$ is 9.01 µPa s at 298K and 4.7 MPa[48] and the IFT between $H_2$ and water is 72.6 mN $m^{-1}$ at 298K and 5 MPa[49, 50]). Subsequently, the brine was reinjected (imbibition) at flow rates of 20-

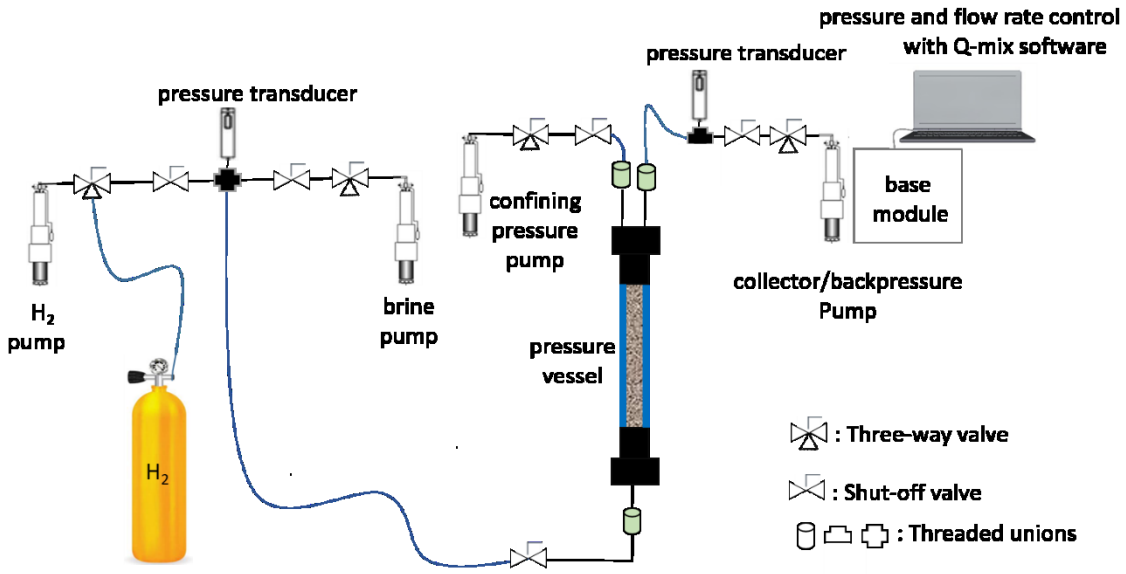


Figure 1: Experimental setup showing the manifold system that connected the X-ray transparent pressure vessel to a set of four high-pressure Cetoni Nemesys™ pumps: one to inject $H_2$, one inject brine, one to maintain backpressure and one to maintain confining pressure. The materials for the connections were 316 stainless steel (black), HPLC (green) and PEEK or carbon fibre reinforced PEEK (blue). The pressure vessel consisted of carbon fibre reinforced PEEK in UoE experiments and of aluminium in the dry rock experiment (see text). Pressure and flow rate control was achieved with the Q-mix software.

80 µl $min^{-1}$, resulting in $N_C$ of 2.35-9.45x$10^{-6}$ (using the same IFT between $H_2$ and water of 72.6 mN $m^{-1}$ at 5 MPa and 298 K[49, 50] and a viscosity of 1.247 Pa s at 5 MPa that was estimated from the reported 1.2503 Pa s and 1.233x$10^{-3}$ Pa s at 0.1 MPa and 25 MPa, respectively, and 298 K[51]). The $N_C$ the $N_2$ experiment was 3.5x$10^{-8}$ (using an IFT of 73 mN $m^{-1}$ between $N_2$ and water 1t 298K and 10 MPa[35] and a viscosity of 1.89x$10^{-5}$Pa s at 5 MPa and 295K[48]). Each injection used ten pore volumes to ensure completely flushing of the sample cores with the injected fluid.

In the dry rock experiment, $H_2$ was directly injected into a dry rock at a flow rate of 70 µl $min^{-1}$. Subsequently, the brine (2 M KI) was injected at a flow rate of 5 µl $min^{-1}$, resulting in $N_C$ of 5x$10^{-7}$ (using the same IFT between $H_2$ and water of 72.6 mN $m^{-1}$ at 5 MPa and 298 K[49, 50] and a viscosity of 1.07x$10^{-3}$Pa s for 0.6 M KI and 293 K[42]).

The combined application of an x-ray transparent core holder and μCT allowed the visualization of the fluid saturation distributions at pore scale at each injection step. The difference in the x-ray attenuation coefficient of the fluids ($H_2$ and 0.5 M CsCl/ 2 M KI) provided an excellent contrast between the two fluid phases and the rock on the acquired μCT images, combined with the respective radiation energy in the two different laboratories.

3D volumes were acquired from the lower central portion of the sample to avoid the impact of capillary end effects on fluid saturation[46, 47]. For the UoE experiments, image acquisition used a μCT instrument built in-house at the University of Edinburgh, comprising a Feinfocus 10-160 kV reflection source, a Micos UPR-160-air rotary table and a Perkin-Elmer XRD 0822 1 MP amorphous silicon flat panel detector with a terbium doped gadolinium oxysulfide scintillator. Data acquisition software was developed in-house. The following settings were used for UoE experiments: 120 keV, 16 W, 2 seconds exposure time, 1200 projections and 2 frames per stop. The voxel size was 5.4 $\mu m^3$. In the dry rock experiment, time-resolved imaging of the $H_2$ and brine displacement processes was achieved by means of a 65 keV monochromatic beam detected by a high-resolution imaging camera with optical module 2 (PCO.edge 5.5, 7.91 x 7.9 μm/pixel with FoV 20 mm x 12 mm) using 17-25 milliseconds exposure time and 900 projections. The voxel size was 7.9 $\mu m^3$.

*2.2 Image analysis*

Tomographic reconstructions were undertaken by filtered back projection using Octopus 8.9[52] on a GPU accelerated workstation. All subsequent image processing and analysis of tomographic data was performed using Avizo Version 9.1.1 (FEI, Oregon, USA). Data from UoE experiments were processed using a non-local means filter[53]. Processing of the dry rock experiment used a combination of median filter and unsharp mask to reduce image noise.Segmentation of UoE experiment data used a global threshold on the 2D greyscale image histogram, and encompassed two phases. In the water-saturated scans, water and rock were

treated as two discrete phases. In scans after brine and $H_2$ injections, the $H_2$ was treated as one phase and the brine and rock as a single separate phase, following protocols of Andrew et al. (2014)[32]. Holes and spots which were at the resolution limit of the data were removed from all datasets (applied thresholds corresponded to $3^3$ and $5^3$ voxels, respectively). Based on the segmented image of the water-saturated scan in UoE experiments, a pore size distribution was calculated. The 3D image was separated into individual pores and throats using Avizo's 'separate objects' module, which calculates a chamfer distance map of the pore-space and then applies a marker based watershed algorithm to the distance map to define discrete pore bodies as catchment basins separated by the watershed which marks the location of pore throats (SI Figure S1d). Supporting information Figure S1 shows the work flow for the water-saturated scan.

In scans following brine and $H_2$ injections in UoE experiments, the segmented image was analysed in 3D using the 'labeling' and 'label analysis' modules to identify, label and measure the volume of each $H_2$ cluster. Hydrogen cluster size distributions were compared to the pore size distribution to evaluate the $H_2$ connectivity and identify trapping mechanisms during brine imbibition.

*2.3 Capillary pressure*

Recovered Clashach cores were submerged in 25% w/v NaOH solution (Fisher Scientific) for 2 hours to remove the aluminium foil from the core surface, and rinsed in successive milli-Q water, acetone and ethanol ultrasonic baths. Subsequently, the cores were cut and squared to the dimensions of 25 mm, overlapping the μCT visualized rock volumes, and cleaned ultrasonically with milli-Q water to remove grinding products. Mercury injection capillary pressure (MICP) was performed on the cleaned cores, using a micromeritics automated mercury injection equipment (Autopore IV 9500) to estimate the capillary pressure-saturation relationship and pore size distribution. The pressure range tested was from vacuum to 379 MPa.

253 **3. Results**

254 *3.1 Characterization of the pore space*

255 The µCT-evaluated porosity of the
256 Clashach sandstone from the segmented
257 volume of the water-saturated rock was
258 12.5% to 13.5%, depending on the imaged
259 region of the rock core. The MICP-
260 evaluated pore throat size distribution
261 showed a large number of very small pore
262 throats with <5 µm radius and a small
263 number of small to intermediate size pore

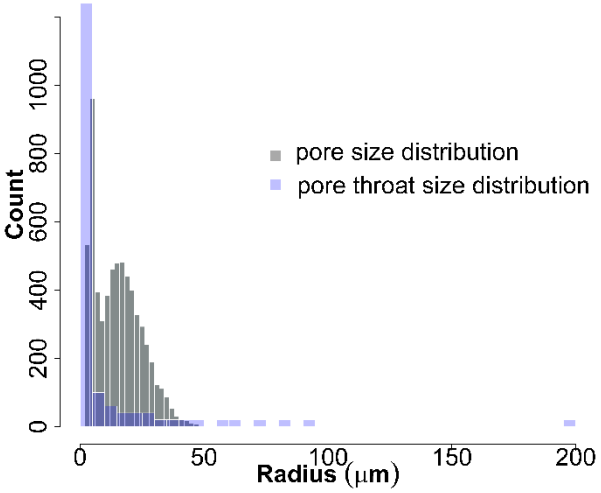


Fig. 2. µCT-derived pore size distribution (grey) and MICP-derived pore throat size distribution (transparent blue). Note that MICP derived counts were multiplied by a factor of 20 to facilitate visualization of the results. All plots used a bin size of 30.

264 throats (>5 to 90 µm) (Fig. 2). The largest pore throat had a radius of 195 µm (Fig. 2). The
265 µCT-evaluated size distribution of the pores evidenced a narrow pore size distribution with
266 comparably small pores with radii <50 µm (Fig. 2, 4a).

267 *3.2 Hydrogen wetting behaviour and stability in UoE experiments*

268 Hydrogen sat in the centre of the pore bodies. Residual brine sat in corners, pore throats (Fig.
269 3b and c) and, as a subtraction of the water saturated scan from the $H_2$-and brine filled rock
270 revealed, in thin films around the grains (Fig. 3d). The injected $H_2$ remained stable within the
271 pore volume under no-flow conditions and at constant pore fluid pressure over a time period
272 of 10 hours which was the maximum experimental duration (SI Fig. S2).

273 *3.2 Effect of pore fluid pressure on hydrogen connectivity, saturation and recovery*

274 Hydrogen saturation during drainage was independent of the pore fluid pressure with 49.8%,
275 51.7% and 39.7%-52.6% saturation at pore fluid pressures of 2, 5 and 7 MPa, respectively (Fig.
276 4a-c, f, SI Fig. S3). Hydrogen connectivity during drainage generally showed one large,

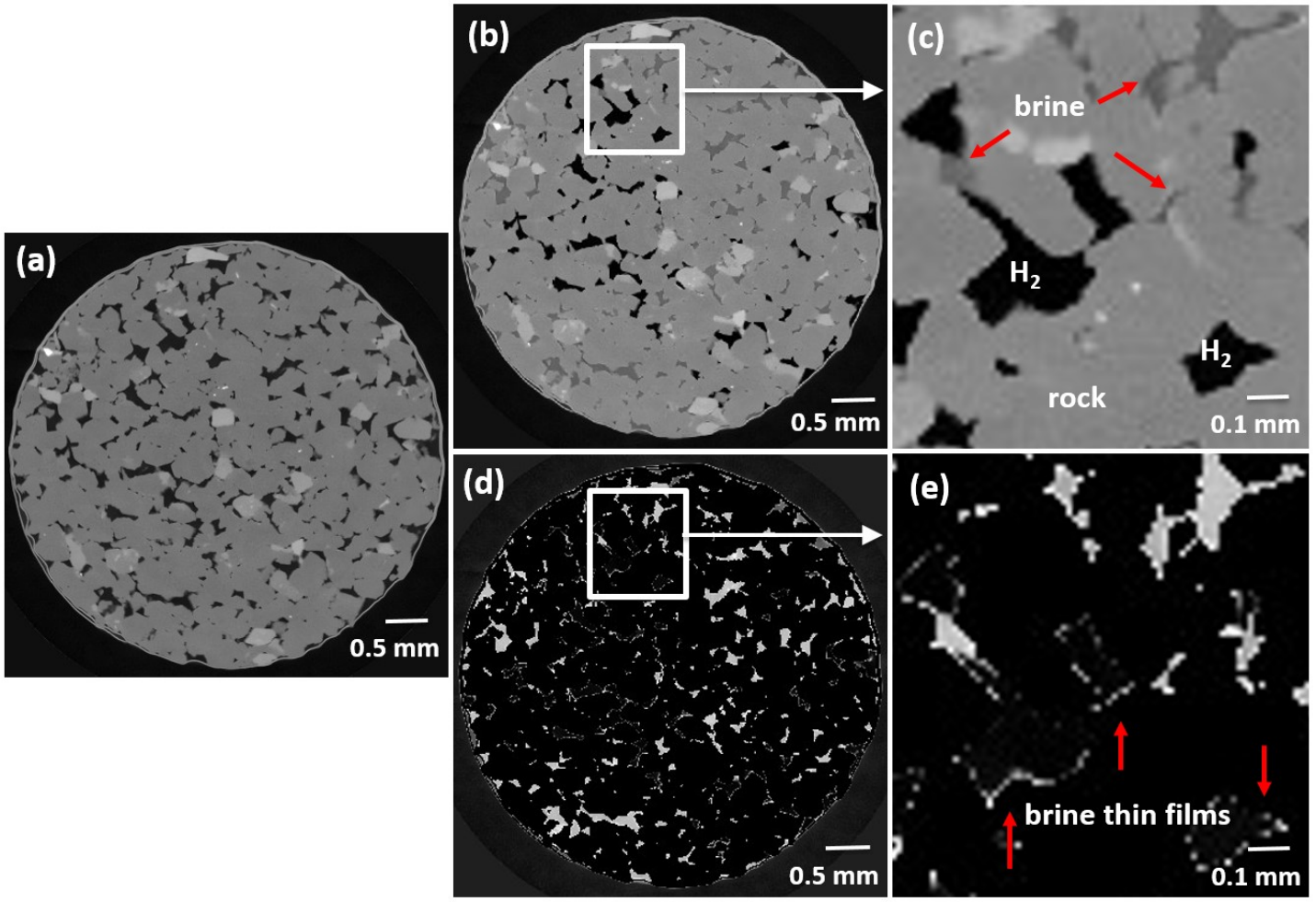


Fig. 3: **(a)** Water-saturated Clashach sandstone with the water shown in black and the rock in different shades of grey. **(b)** and **(c)** Brine-saturated Clashash sandstone after injection of $H_2$. $H_2$ (black) fills the centre of the pores while the brine (dark grey) remains in corners and small pore throats around grains. **(d)** and **(e)** Subtraction of the water-wet scan from the brine-saturated scan after $H_2$ injection, following registration of the brine-saturated scan after $H_2$ injection to the water-saturated scan, revealing discontinuous brine thin films around grains. The rim around the Al foil in **(d)** is caused by continued shrinkage of the Al foil onto the rock during the experiments.

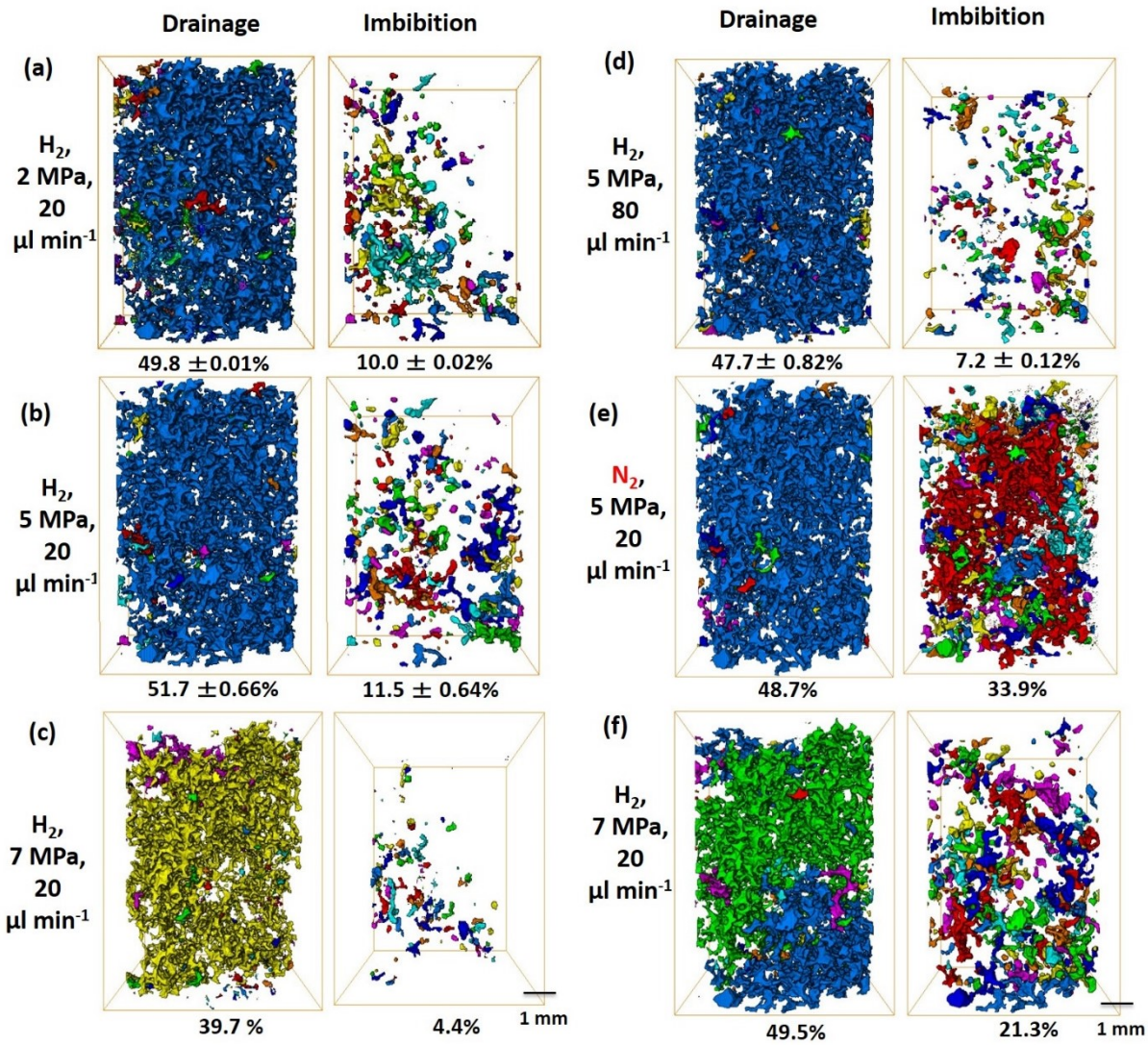


Fig. 4: 3D rendering of $H_2$ and $N_2$ clusters with saturation percentages in UoE experiments. Discrete clusters were rendered in colours, where mainly one color marks one large, connected cluster and different colors indicate several, not connected clusters. **(a-c)** Effect of pore fluid pressure on $H_2$ clusters and saturation after drainage and after primary imbibition. **(a)** 2 MPa, **(b)** 5 MPa and **(c, f)** 7 MPa, all at a constant flow rate of 20 µl $min^{-1}$ corresponding to capillary numbers of $1.7x10^{-8}$ and $2.4x10^{-6}$, respectively. Large, connected clusters that existed after drainage were broken down to numerous smaller clusters after imbibition, with apparently no clear relationship between $H_2$ saturation and pore fluid pressure. Experiments were repeated once at 2 and MPa, and at 7 MPa twice for drainage runs and once for imbition. For experiments at 2 MPa and 5 MPa averages and standard errors for the $H_2$ saturation are reported. For experiments at 7 MPa, due to the discrepancy in the results, both of the full primary drainage and imbibition experiments are visualized in **(c)** and **(f)**. **(d)** Effect of cyclic injections on $H_2$ clusters and saturation: Averages and standard errors of the $H_2$ saturation after primary and secondary drainage, and after primary and secondary imbibition, all at 5 MPa pore fluid pressure and a flowrate of 80 µl $min^{-1}$ corresponding to a capillary number of $9.4x10^{-6}$. **(e)** Nitrogen clusters and saturations during drainage and imbibition at 5 MPa pore fluid pressure and a flowrate of 20 µl $min^{-1}$. For the full display of the results see SI Fig. S3 and SI Fig S4.

connected cluster at all pore fluid pressures except for one out of three images at 7 MPa which showed three large disconnected clusters (Fig. 5, SI Fig. S3). During drainage, the largest $H_2$ cluster had a volume of $1x10^8$ $\mu m^3$ at all pore fluid pressures except for the one run at 7 MPa with the disconnected clusters were the largest volume was $7x10^7$ $\mu m^3$ (Fig. 5e).

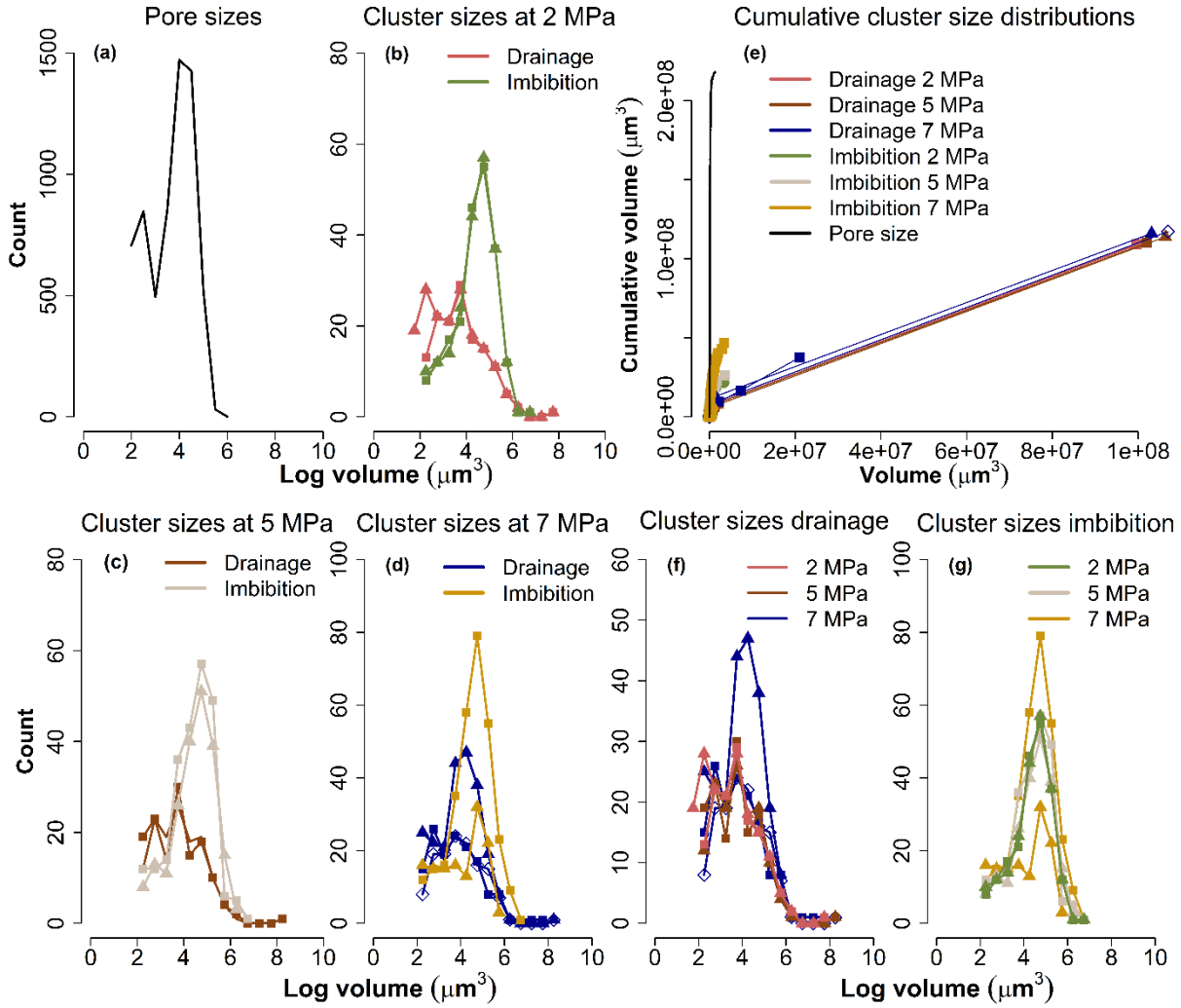


Fig. 5: **(a)** Pore size distribution as derived from the micro-CT image of the water-wet rock. Hydrogen cluster size distributions after drainage and imbibition in experiments at 20 µl $min^{-1}$ flowrate and pore fluid pressures of 2 MPa **(b)**, 5 MPa **(c)** and 7 MPa **(d)**, and cumulative pore size and $H_2$ cluster size (CS) distributions at different pore fluid pressures **(e),** where squares, triangles and rhombi mark the distinct repeat experiments. **(f)** Hydrogen cluster size distribution after drainage for all experiments and **(g)** Hydrogen cluster size distribution after imbibition for all experiments. Note the large $H_2$ clusters of ~$10^8$ $\mu m^3$ that exist after drainage in **(b)**-**(d)**. A decrease in the biggest cluster volume after imbibition in **(b)**-**(d)** along with an increase in the number of small clusters marks the change in $H_2$ structure during the drainage and imbibition processes. Histogram plots in **(a)**-**(d)**, **(f)** and **(g)** used a bin size of 10.

304 Hydrogen clusters during drainage were at all pore fluid pressures much larger than discrete
305 pores with a maximum volume of $1.3x10^6$ $\mu m^3$ (Fig. 5e, a). Comparing all $H_2$ cluster size
306 distributions during drainage (Figure 5f) reveals that all drainage curves, including two of the
307 distributions at 7 MPa (squares and rhombi), have largely the same distribution, however one
308 of the three distributions at 7 MPa (triangles) is distinct. This outlier experiment corresponds
309 to the experiment showing a lower $S_{nwi}$ (Fig. 4c).

310 Capillary trapping of $H_2$ during imbibition seemed independent of the pore fluid pressure with
311 10%, 12% and 4-21% of trapped $H_2$ at 2, 5 and 7 MPa, respectively (Fig. 4a-c,f, SI Fig. S3),
312 corresponding to 20%, 22% and 11-43% of the initially injected $H_2$. During imbibition, large
313 $H_2$ clusters were broken down into smaller clusters (Fig. 5a-d), in line with the visual changes
314 of the $H_2$ clusters (Fig. 4a-c and f). The largest $H_2$ clusters after imbibition remained above the
315 maximum pore size during all experiments except for one experiment at 7 MPa (triangles in
316 Fig. 5g, Fig. 5a), showing that not only was $H_2$ trapped in discrete pore bodies but also as larger
317 $H_2$ ganglia. The break-down of the largest $H_2$ clusters during imbibition caused the number of
318 clusters in the size range log 4 to log 6 $\mu m^3$ to increase while the number of very small clusters
319 of log 2-4 $\mu m^3$ typically decreased (Figs. 5b-d). Comparing all $H_2$ cluster size distributions
320 during imbibition (Figure 5g) shows that the distributions at 2 and 5 MPa are largely the same
321 while the imbibition distributions at 7 MPa are distinct.
322 Injections of $H_2$ and brine into the same rock volume and at the same flow rates and pore fluid
323 pressures of 2-5 MPa were repeatable with small standard errors between 0.01-0.66% (Fig. 4a
324 and b, Fig. 5b and c). At 7 MPa very distinct $S_{nwi}$ and $S_{nwr}$ were measured (Fig. 4c and f); During
325 drainage the standard error was 4.8% at an average $H_2$ saturation of 47.4%. The standard error
326 during imbibition was 8.5% at an average saturation of 12.9%. The pressure differences
327 between inlet and outlet during these experiments were within the error of the pressure sensors

of 0.1% full-scale.

*3.3 Effect of hydrogen/brine injection ratio on hydrogen connectivity and saturation*

We studied the effect of the $H_2$ /brine injection ratio on the $H_2$ saturation in order to evaluate the effect of $H_2$ injection into hydrodynamic aquifers, and to evaluate what happens in the far field, where fluids will be moving together. The results showed that the $H_2$ saturation and $H_2$ interconnected pore volume increased with increasing $H_2$/brine injection ratio from 32.6% at 4 µl $min^{-1}$ $H_2$ plus 16 µl $min^{-1}$ brine to 43.2% at 16 µl $min^{-1}$ $H_2$ plus 4 µl $min^{-1}$ brine (Fig. 6). The $H_2$ clusters in simultaneous injection experiments occupied many of the same pore spaces as the clusters after $H_2$ in the non-steady state experiments at the same pressure and total flowrate (Fig. 4b, Fig. 6, SI Fig. S5), and even at the lowest $H_2$ brine injection ratio of 4 µl $min^{-1}$ $H_2$ plus 16 µl $min^{-1}$ brine, the $H_2$ clusters were large, and spanning multiple pores. The percolation threshold, i.e. one connected path from inlet to outlet, was apparently only reached at 100% $H_2$ injection (Fig. 4b vs. Fig. 6, SI Fig. S5). The pressure

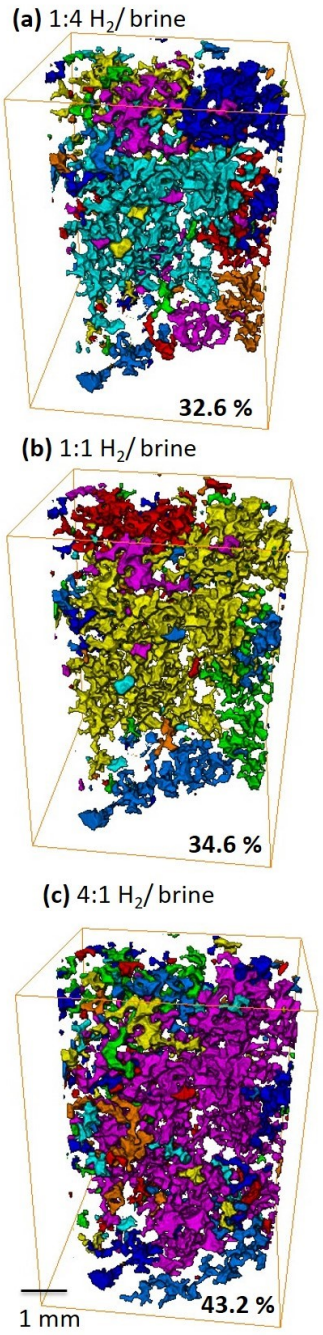


Fig. 6: Effect of $H_2$/brine injection ratio on $H_2$ saturation and $H_2$ connectivity during simultaneous $H_2$ and brine injection at 5 MPa **(a)** 4 µl $min^{-1}$ $H_2$ plus 16 µl $min^{-1}$ brine, **(b)** 10 µl $min^{-1}$ $H_2$ plus 10 µl $min^{-1}$ brine, **(c)** 16 µl $min^{-1}$ $H_2$ plus 4 µl $min^{-1}$ brine. Discrete $H_2$ clusters were rendered in colours, where mainly one color marks one large, connected cluster and different colors indicate several, not connected clusters. With increasing injection ratio $H_2$ saturation and $H_2$ connectivity increase.

differences between inlet and outlet during the simultaneous injection experiments were up to 0.05 MPa.

The $H_2$ cluster volume distributions were similar at different $H_2$:brine injection ratios (Fig. 7a). However, with increasing ratio the smallest $H_2$ clusters of volume ~log 2 $\mu m^3$ decreased in number while the number of intermediate size (log 2.5 to log 6.25 $\mu m^3$) $H_2$ clusters and the volume of the biggest cluster increased (Fig. 7a), confirming observations of increasing $H_2$ saturation and connectivity with increasing injection ratio (Fig. 6).

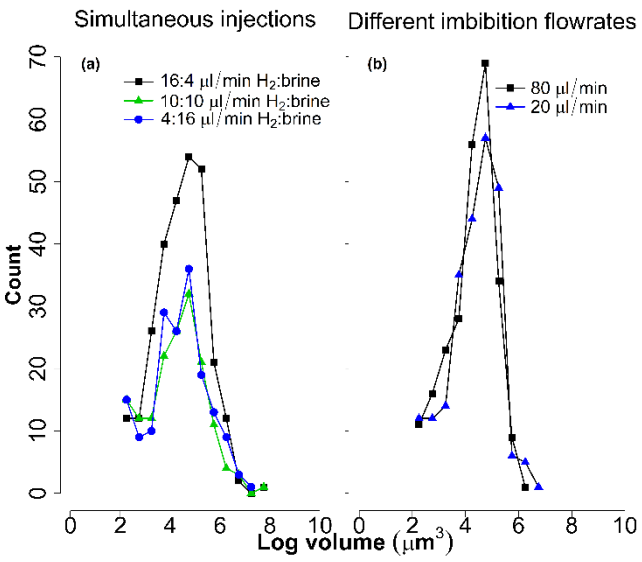


Fig. 7. **(a)** $H_2$ cluster size distributions during simultaneous injections of $H_2$ and brine at flowrate ratios of 16:4, 10:10 and 4:16 µl $min^{-1}$ $H_2$:brine and 5 MPa injection pressure. As the flowrate ratio of $H_2$ to brine increased, the number of intermediate size $H_2$ clusters increased and the radius of the biggest cluster increased. **(b)** Effect of flowrate during brine imbibition. All plots used a bin size of 10.

*3.4 Effect of flowrate on hydrogen saturation and recovery*

At constant pore fluid pressure of 5 MPa, increases in the flowrate during drainage from 20 µl $min^{-1}$ to 80 µl $min^{-1}$, corresponding to bulk $N_C$ of 1.7 $x10^{-8}$ to 6.8$x10^{-8}$, respectively, decreased the $H_2$ saturation from to 51.7% to 47.7% (Figure 4b and d). Correspondingly, increases in the brine flowrate during imbibition from 20 µl $min^{-1}$ to 80 µl $min^{-1}$, corresponding to bulk $N_C$ of 2.4$x10^{-6}$ and 9.4$x10^{-6}$, respectively, reduced the $S_{nwr}$ from 11.5% to 7.2% (Fig. 4b and d). In line with this, the $H_2$ cluster size distributions at the two flowrates showed that larger clusters were mobilized at 80 µl $min^{-1}$ (maximum cluster sizes of log 6.25 $\mu m^3$ at 80 µl $min^{-1}$ vs. log 6.75 $\mu m^3$ at 20 µl $min^{-1}$; Fig. 7b). At both flowrates the largest $H_2$ clusters were still bigger than

the largest pore of <log 6 $\mu m^3$ (Fig. 7b vs. Fig 6a), indicating that $H_2$ was trapped also as larger ganglia.

*3.5 Secondary drainage and imbibition*

Secondary drainage and imbibition did not significantly change the $H_2$ saturation (47.9% and 7.0%) compared to primary drainage and imbibition (47.6% and 7.3%), based on results at 5 MPa and 80 $\mu l\ min^{-1}$ flowrate (SI Fig. S4, Fig. 4d-e).

*3.6 Dry rock experiment*

In the dry-rock experiment, the brine entered the $H_2$-filled dry rock via piston-like displacement, (Fig. 8b), eventually recovering the $H_2$ entirely (Fig. 8d). Before all $H_2$ was recovered, there was an intermediate stage where previously brine-filled pores (Fig. 8b) showed several very small $H_2$ bubbles (Fig. 8d).

*3.7 Comparison to nitrogen*

The $N_2$ saturation was similar to the $H_2$ saturation during drainage (48.7% vs. 51.7 ± 0.66%, respectively) but $N_2$ saturation after brine imbibition was much higher (33.9% vs. 11.5 ± 0.64%, respectively; Fig. 4e, SI Fig. S6). The $N_c$ of $H_2$ and $N_2$ during drainage were $1.7x10^{-8}$ and $3.5x10^{-8}$, respectively.

## 4. Discussion

*4.1 Pore space*

The µCT-evaluated porosity of the Clashach sandstone from the segmented volume of the water-saturated rock of 12.5-13.6% was within the range of the published porosities of 11.1-14.4% for Clashach sandstone[42-44]. The distributions of pore size and pore throat size as evaluated by µCT and MICP, respectively, suggested that mostly small pores of <50 µm radii were joined by very small throats of <5 µm radii with a few small to intermediate size throats

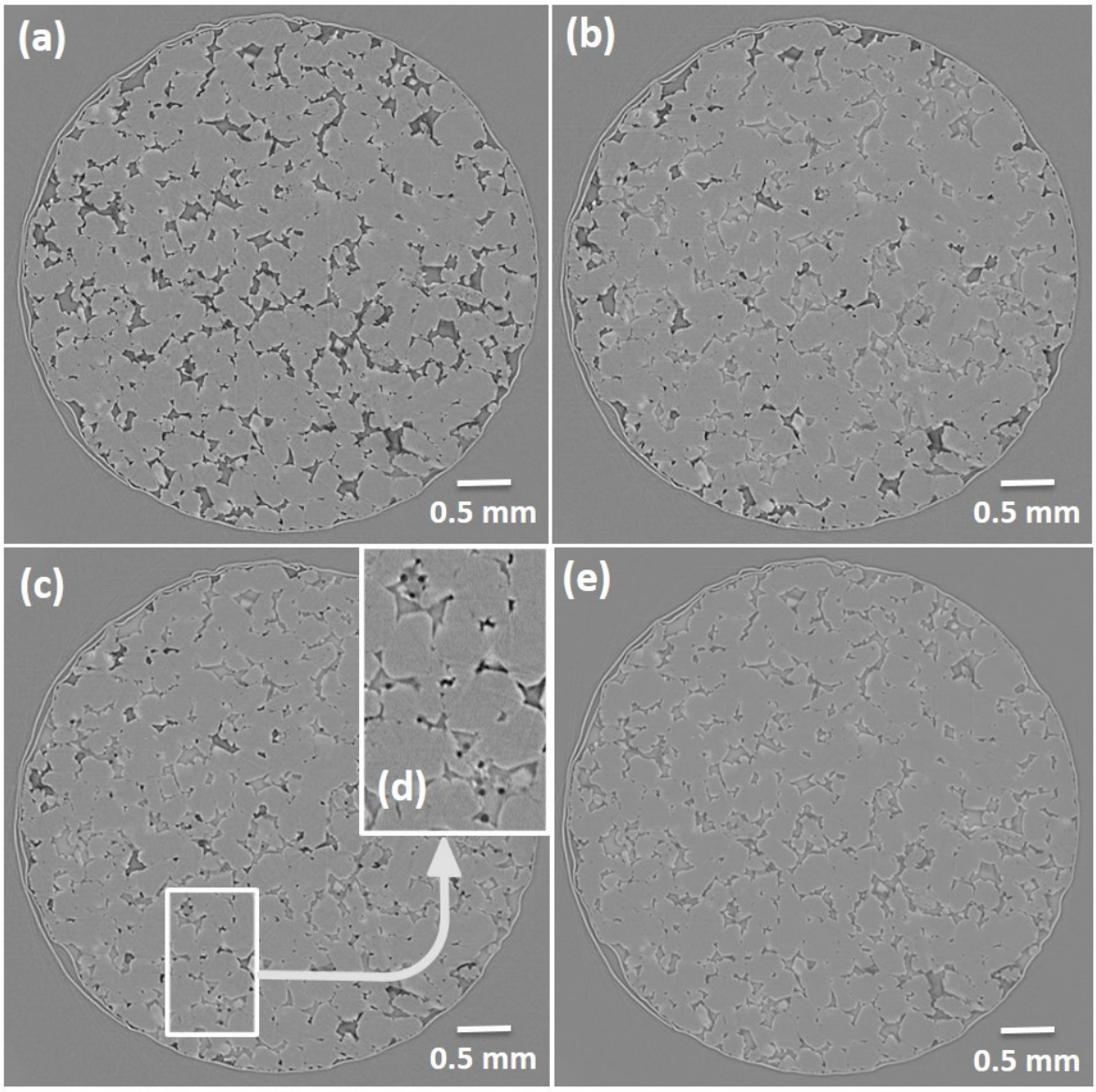


Fig. 8. The dry-rock experiment summarized. **(a)** $H_2$-saturated, dry rock, **(b)** scan during brine imbibition shortly after appearance of the first brine in the rock, **(c)** scan during brine imbibition after 115 minutes, with several small, isolated $H_2$ bubbles inside pore bodies **(d),** and **(e)** brine-saturated rock after two hours of imbibition showing 100% recoverability of $H_2$.

of >5 to 90 µm radii in between (Fig. 2). The largest pore throat of 195 µm radius was probably measured at the surface of the rock core where the drilling process affected the pore space. The pore throat distribution for our Clashach sandstone sample was very similar to the pore throat distribution for Berea sandstone[54]. Compared to the pore throat distributions for Bentheimer

411 sandstone and Doddington sandstone[54], our Clashach sandstone sample showed smaller pore
412 throat sizes. Limestones generally show a wider pore throat size distributions than sandstones[54].

413 *4.2 $H_2$ flow behaviour and trapping mechanisms*

414 Hydrogen behaved as a non-wetting phase, filling the centre of the pores, with residual brine
415 in the pore corners and throats (Fig. 3b and c), indicating a water wetting system. The largest
416 $H_2$ cluster was much larger than discrete pores at any pore fluid pressure during drainage (Fig.
417 5), indicating a good connectivity of the $H_2$[55]. Hydrogen trapping occurred via snap-off of $H_2$
418 ganglia (Fig. 9). Snap-off competes with piston-like, i.e. pore-filling, displacement during the
419 displacement of a non-wetting fluid by a wetting fluid in porous media[21], and is known as the
420 swelling of water in the corner layers of a pore throat during water invasion in water-wet porous
421 rocks until the threshold capillary pressure is exceeded, resulting in spontaneous filling of the
422 throat with water and disconnection of the non-wetting phase which can lead to trapping[21].
423 Brine films around grains were not directly visible in the tomographic images (Fig. 3b and c)
424

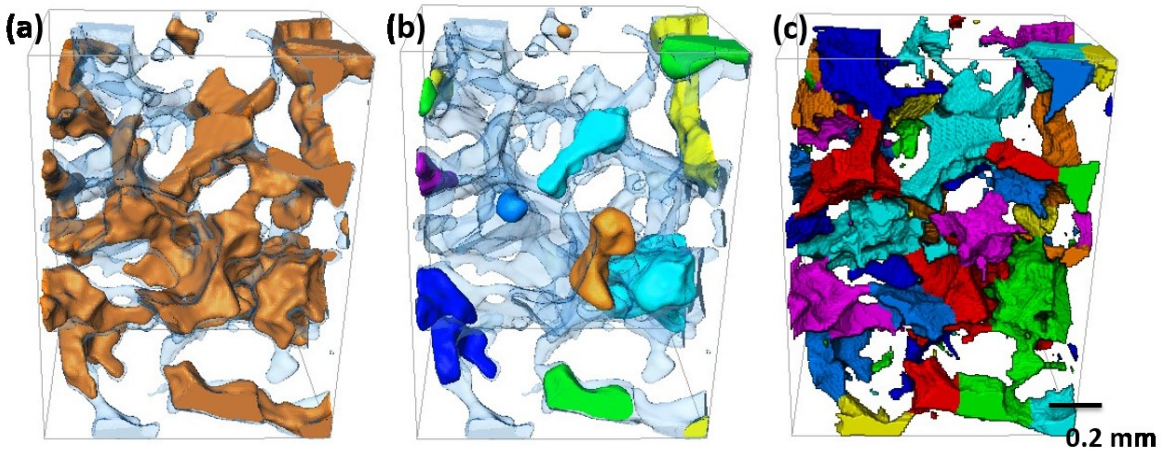


Fig. 9: Example of a snap-off event. **(a)** Labelled $H_2$-filled volume after drainage (orange), spanning over several pores, and total pore space (transparent blue) showing one large interconnected $H_2$-filled pore volume. **(b)** Labelled $H_2$-filled volume after brine imbibition (different coloured shades) and the total pore space (transparent blue) showing several, not connected $H_2$ ganglia and the snapped-off $H_2$ droplet (cobalt blue) in the centre, left hand side. **(c)** Pore body visualisation of the same volume.

but were revealed by subtraction of the water-saturated scan from the brine-saturated scan after $H_2$ injection, following the registration of the brine-saturated scan after $H_2$ injection to the water-wet scan (Fig. 3d and e). Figures 3d and 3e suggest that brine films were discontinuous and very thin. When $H_2$ was injected into a dry rock, 100% of the injected $H_2$ could be recovered (Fig. 8e) which substantiated the theory that sub-resolution brine films around grains and snap-off of $H_2$ ganglia caused decreased $H_2$ recovery in experiments using an initially brine saturated rock (UoE experiments). The occurrence of several very small $H_2$ bubbles in the dry-rock experiment (Fig. 8d) indicated Roof snap-off[56] of $H_2$ ganglia.

*4.3 Effect of pore fluid pressure and hydrogen/brine injection ratio*

We observed no dependence of the $H_2$ saturation during drainage on pore fluid pressure, considering that 2 out of 3 experiments at 7 MPa showed the same the same $H_2$ saturation of ~50 % as at 2 and 5 MPa (Fig. 4a-c,f, and SI Fig. S3). The one experiment at 7 MPa which had only 39.7% $H_2$ saturation (Fig. 4c, SI Fig. S3 and blue triangles in Fig. 5f) did also not have the same $H_2$ cluster size distribution as the remaining experiments (Fig. 5f), despite using the same experimental settings as for all other experiments at 7 MPa, and the log archives of the pore fluid pressures and injected volumes revealed no abnormalities. A shift in the distribution of cluster sizes can indicate a change in wettability, regardless of the measured $H_2$ saturation. Yet, as two of the results at 7 MPa showed a similar distribution as at the other pressures, it seems likely that this experiment is an outlier. The experiment was acquired after a filament change on the µCT apparatus, which implied that a slightly different part of the same rock core was imaged (13.6% vs. 12.5% porosity). Yet, in principle this should not have affected the results significantly, and subsequent experiments did return to show ~50% $H_2$ saturation, e.g. the $H_2$ stability experiment (SI Fig. S2).

The observed constant drainage $H_2$ saturations with increasing pore fluid pressures from 2 to 7 MPa are in line with a lack of a dependence of the $H_2$ wettability on pressure increases from 2-

450 10 MPa in Berea and Bentheimer sandstone[18], with only very small increases of ~3-6° in the
451 $H_2$ contact angles at pressure increases from 2 to 7 MPa in Basalt[21] and clay[24] and quartz[19], and
452 with a previous findings of no change in the characteristic trapping curves for $CO_2$ and $N_2$ at a
453 wide range of pressure and temperature conditions[35]. The general anticipation of an increase in
454 gas saturation with injection pressure[57, 58] may still be valid over pressure ranges larger than
455 the one investigated here. At unchanged wettability, the $S_{nwi}$ is controlled by the capillary
456 pressure which in turn is controlled either by the fractional flow (during simultaneous injection)
457 or by the viscous force pressure drop (during single fluid phase injection). Thus, the
458 independence of the $S_{nwi}$ from the pore fluid pressure indicates that the viscous pressure drop
459 is not being significantly altered by the changing pressure, e.g., the $H_2$ viscosity change is not
460 having a major impact on the force required to drive flow. Significant loss of $H_2$ from the gas
461 phase at higher pressures by dissolution into the brine is precluded by the low solubility of $H_2$
462 of ~0.02 mol $kgw^{-1}$ at 2.5 MPa[59]. The $H_2$ stability experiments showed that $H_2$ saturation at 5
463 MPa did not change over a time period of ten hours (49.55% at time zero vs. 49.53% ten hours
464 after; SI Fig. S2), evidencing a stable result and no $H_2$ loss by dissolution.
465 Looking at the $S_{nwr}$ data only (Fig. 4a-c,f), there was no clear dependency on pore fluid pressure
466 during imbibition. Any change may, however, have been masked by the high variation between
467 the two results at 7 MPa (4-21% Fig. 4c and f). Considering that the experiment at 7 MPa with
468 the low $S_{nwi}$ of 40% could be identified as an outlier (see the discussion in the beginning of
469 section 4.3, and Fig. 5f, blue triangles) and that the $S_{nwr}$ is a function of the $S_{nwi}$ where a lower
470 $S_{nwi}$ will tend to overestimate recovery[54, 60], we may disregard the $S_{nwr}$ of 4%. The large increase
471 in trapped $H_2$ in the second full primary drainage and secondary imbibition experiment at 7
472 MPa (Fig. 4f) was probably due to the poorer intial $H_2$ connectivity[60]. The $H_2$ cluster size
473 distribution for this experiment showed an increase in the number of intermediate size clusters
474 compared to the other experiments (Fig. 5g, darkyellow squares), without however shifting the

cluster distribution, suggesting no wettability change. This indicates that variation in one or more of the other thermophysical properties –density, viscosity, or IFT – have resulted in the impact on the pore scale fluid configuration (Figure 10). Meanwhile, a poorer initial $H_2$ connectivity was not confirmed by the third repetition of primary drainage at 7 MPa (SI Fig. S3g). More experiments at 7 MPa are needed to confirm the result of increased trapping at higher pore fluid pressures.

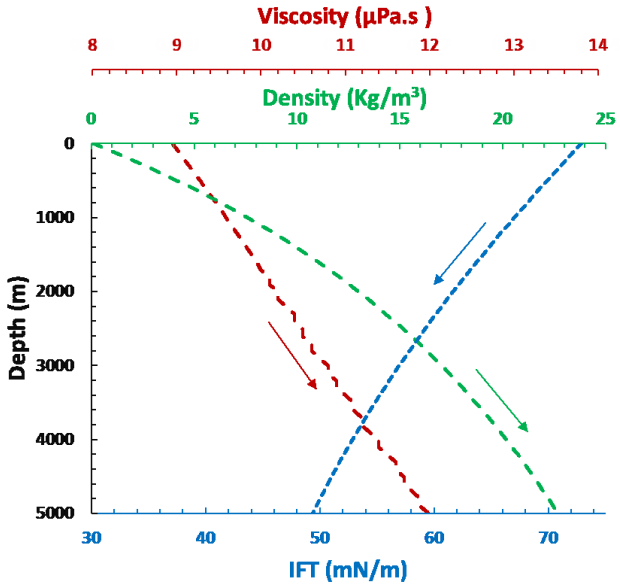


Fig. 10: Density (green line), viscosity (red line), and interfacial tension (blue line) of hydrogen versus depth (Hassanpouryouzband et al. 2021)[61].

Given a hydrostatic gradient of ~10 MPa/km an increase of the $S_{nwr}$ with increasing pore fluid pressure, as suggested by the second experiment at 7 MPa (Fig. 4f), would indicate that deeper aquifers are less favourable for $H_2$ storage operations. However, unlike our non-steady state experiments which showed barely any pressure difference between inlet and outlet, in a real $H_2$ storage operation, the well pressure is significantly higher than the reservoir pressure and the brine is not injected, but naturally flowing into previously $H_2$-saturated rock when the $H_2$

is recovered- again due to a pressure difference. Our displacement study results are hence applicable to the fringe of the $H_2$-saturated zone, only, where pressure differences are very small. A decreased $H_2$ recovery with depth would not align well with other criteria for an economical and safe $H_2$ storage operation, such as a lower cushion gas requirement with elevated depth[5] and reduced risks for $H_2$-linked microbial activity at higher depths due to higher temperatures[6].

The pressure/depth effect on our results can be further related to the variation of key pore-scale displacement parameters for $H_2$ with depth (Fig. 10): The IFT of $H_2$ reduces with depth whereas the $H_2$ viscosity increases, both of which in theory should augment the displacement of $H_2$ with water and reduce the $S_{nwr}$[62, 63]. However, increased $S_{nwr}$ with decreasing IFT and increasing viscosity has also been demonstrated[64] which may be due to a simultaneously increased likelihood of unstable displacement/ non-uniform fronts[10, 65] during both drainage and imbibition processes at decreasing IFT and increasing viscosity, based on the augmenting effect of both parameters on $N_C$ (Eq. 1). Such unstable displacement processes at higher pore fluid pressures, addition to a variation in the thickness of the brine thin films with pressure, may explain the decrease in interconnected $H_2$-filled pore volume from one large cluster at 2-5 MPa to three clusters at 7 MPa and have lead to increased snap-off and trapping during imbibition (Fig. 4f).

The $S_{nwr}$ of 10-21% was significantly less than the previously reported $H_2$ $S_{nwr}$ of 41% for a sandstone under ambient conditions[40]. As mentioned previously, the short length rock sample in Jha et al. (2021)[40] suggests that their results were affected by capillary end effects[46]. However, the applied the relatively high bulk brine $N_C$ of $2.4 \times 10^{-6}$ may have mobilised more residual $H_2$ than under strict capillary regime conditions.

During simultaneous injection of $H_2$ and brine, which may be representative of $H_2$ injection into hydrodynamic aquifers or simulate the far field conditions, $H_2$ saturation and $H_2$

514 interconnected pore volume increased with increasing $H_2$/brine injection ratio (Fig. 6). This
515 indicated that a lower brine flow is favoured over high flow environments in terms of
516 optimising the $H_2$ storage operation. The structure was apparently not percolating in any of the
517 simultaneous injection experiments as opposed to during 100% $H_2$ injection (Fig. 6 vs. Fig.
518 4b), yet considering significant pressure differences of up to 0.05 MPa between inlet and outlet
519 in simultaneous injection experiments which were not observed in experiments injecting 100%
520 $H_2$, the connections between the $H_2$ clusters may have been broken when the injection (and
521 thereby the pressure gradient) was stopped for the scan.

522 *4.4 Effect of capillary number on initial and residual saturation*

523 Classical pore-scale displacement theory predicts little change in residual phase saturation in
524 response to increases in flow rate until $N_C$ exceeds $10^{-6}$ -$10^{-5}$. However, for most subsurface
525 reservoirs there will be rapid decreases at $N_C$ of $10^{-4}$ or more, when viscous forces become
526 dominant[54]. The bulk brine $N_C$ applied in this study (2.4-9.4x$10^{-6}$) was within the range of little
527 saturation change but exceeded the threshold of $N_C$ <$10^{-6}$ for which the flow generally is said
528 to be capillary dominated[54]. This may indicate that viscous forces caused a significant effect of
529 $N_C$ on the $S_{nwr}$ in our experiments (Fig. 4b and d), and these forces are likely to be even greater
530 at local scale than at bulk[54]. The $H_2$ cluster size distribution after imbibition at $N_C$= 9.4x$10^{-6}$
531 was shifted with respect to the distribution at $N_C$= 2.4x$10^{-6}$ (Fig. 7b), indicating a change in the
532 wetting behaviour and supporting previous findings of preferential desaturation of larger
533 clusters at higher *Nc*[66].

534 We observed a 4% decrease in $S_{nwi}$ in our experiments when bulk $N_C$ was increased from
535 1.7x$10^{-8}$ to 6.8x$10^{-8}$ (Fig. 4b and d). Critical nonwetting phase $N_C$ of 2x$10^{-8}$ and $10^{-5}$ during
536 imbibition have been reported for water–gas systems and water-oil systems, respectively[67],
537 indicating that the threshold of $N_C$ <$10^{-6}$ for capillary dominated flow[54] is not rigid. However,
538 considering reported increases in the $H_2$ saturation after drainage with increasing $N_C$ from

539 $7.7x10^{-7}$ to $7.7x10^{-5}$ [20], and acknowledging the small observed difference in $S_{nwi}$, we cannot
540 exclude that the effect of flow rate was down to experimental variability.

541 *4.5 Comparison to nitrogen*

542 The $N_2$ saturation was comparable to the $H_2$ saturation during drainage at similar $N_C$ of $1\text{-}3x10^{-8}$
543 but the $S_{nwr}$ after imbibition was ~20 % higher for $N_2$ than for $H_2$ (Fig. 4b and e). Using $N_2$ as
544 a proxy for $H_2$ in experimental drainage and imbibition studies is hence not advisable.
545 Considering the high degree of $N_2$ trapping, the use of $N_2$ as a cushion gas for $H_2$ storage
546 operations which could reduce operational costs[8] seems favourable. Our results are lower than
547 a reported 64% intial $N_2$ saturation during drainage and 43% residual $N_2$ saturation during brine
548 (200 g/L NaI +15 g/L $CaCl_2$) imbibition in a Berea sandstone (20-22% porosity) at 5.5 MPa
549 and 20°C[37], and higher than 43% $N_2$ saturation during drainage in a Bashijiqike tight sandstone
550 (5.6% porosity) at 8 MPa and ambient temperature[36]. The trend in the differences of the $N_2$
551 saturation in the above studies follows the same trend as the differences in the porosities of the
552 studied sandstones, with the Clashach sandstone (14% porosity) being intermediate between
553 the two other rocks. This indicates that porosity differences between the different rock types
554 applied in the above experiments defined the observed $N_2$ saturations, yet differences in the
555 pore throats dimensions may equally have contributed or caused this. Hence $S_{nwi}$ and $S_{nwr}$
556 depend strongly on (the local conditions within) each rock, and these rock type/local effects
557 may mask any effect of injection conditions. However, trends in the rock-specific behaviour
558 will be controlled by pressure and flow conditions. It follows from this that any rock selected
559 for $H_2$ storage operations has to be very well characterized, in particular with respect to
560 porosity, turtoisity and capillary pressure curves.

561 *4.6 Suitability of the Clashach sandstone for hydrogen storage*

562 It has been postulated that the low viscosity of $H_2$ will cause the gas to travel swiftly, making
563 it little suitable for displacing brine[10] and causing low $H_2$ injectivity. In this work, we showed
564 that from an injectivity and recovery perspective, untreated Clashach sandstone is suitable for
565 underground $H_2$ storage. However, sandstones aged by exposure to humic acids may be more
566 suitable analogue rocks for experimental investigations of $H_2$ storage in porous media[19].
567 Considering that aging has previously been shown to alter the wettability of $H_2$ brine-quartz
568 systems from highly water-wet toward intermediate-wet[19] the stated $H_2$ saturations for our
569 untreated outcrop Clashach sandstone are expected to increase during drainage and decrease
570 during imbibition, further the increasing suitability for $H_2$ storage.
571

572 **5. Conclusion**

573 In this work, a prima facie examination of $H_2$ flow and displacement processes in porous rock
574 was carried out as a function of capillary numbers of 1.2-6.8x$10^{-8}$ for $H_2$ and 2.4-9.5x$10^{-6}$ for
575 brine, and of pore fluid pressures between 2-7 MPa. Results showed no clear relation between
576 pore fluid pressure and $H_2$ saturation with ~50% of the pore space saturated with $H_2$ during
577 drainage at all pressures, and 20%, 24% and 43% of the initial $H_2$ trapped at 2, 5 and 7 MPa,
578 respectively, during imbibition at a capillary number of 2.4x$10^{-6}$, indicating that higher
579 pressure, i.e. deeper reservoirs are less favourable for $H_2$ storage. Injection of brine at higher
580 capillary numbers reduced capillary trapping and increased $H_2$ recovery. Hydrogen recovery
581 was distinct from $N_2$ recovery, suggesting that $N_2$ is a poor proxy for $H_2$. Based on these results,
582 we recommend more shallow, lower pressure sites for future $H_2$ storage operations in porous
583 media. Future work should aim to measure the influence of pressures above 7 MPa, elevated
584 temperatures and rock aging on $H_2$ and brine displacement processes at a range of different
585 capillary numbers. Dynamic experiments using synchrotron light sources are recommended to
586 examine displacement mechanisms closely.

## Author Contributions

The experimental kit was built by Butler and Thaysen. Experiments were carried out by Thaysen, Butler, Hassanpouryouzband, Freitas. Alvarez-Borges, Atwood and Humphreys were the supporting beamline scientists during the experiments at Diamond Light Source. Image reconstruction and tomographic analysis was carried out by Thaysen. Interpretation of the results was by Thaysen, Butler, Hassanpouryouzband, Krevor and Heinemann. The manuscript was written by Thaysen with review by Butler, Krevor Heinemann, Hassanpouryouzband, Freitas and Edlmann. All authors have given approval to the final version of the manuscript.

## Declaration of interest

The authors declare no competing interest.

## Funding Sources

Thaysen, Butler, Hassanpouryouzband, Heinemann and Edlmann gratefully acknowledge the funding support from the Engineering and Physical Science Research Council (EPSRC) HyStorPor project [grant number EP/S027815/1] and from the Fuel Cells and Hydrogen 2 Joint Undertaking (JU) under grant agreement No 101006632. The JU receives support from the European Union's Horizon 2020 research and innovation programme and Hydrogen Europe and Hydrogen Europe Research. This work was enabled and carried out with the support of Diamond Light Source, Beamline I12-JEEP 101006632 (proposal mg26730-1).

ACKNOWLEDGMENT

We would like to thank Thomas Connolley for any correspondence and help with setting up the experiments at Diamond Light Source, and Alexis Cartwright-Taylor for assistance and discussions around the experimental results.

613 **References**

614 1. Tarkowski, R., Underground hydrogen storage: Characteristics and prospects *Renew*
615 *Sust Energ Rev* **2020,** *105*, 86-94.
616 2. Beckingham, L. E.; Winningham, L., Critical knowledge gaps for understanding
617 water-rock-working phase interactions for compressed energy storage in porous formations.
618 *Acs Sustain Chem Eng* **2020,** *8* (1), 2-11.
619 3. Mouli-Castillo, J.; Heinemann, N.; Edlmann, K., Mapping geological hydrogen
620 storage capacity and regional heating demands: An applied UK case study. *Appl Energy*
621 **2021,** *283* (116348).
622 4. Hassanpouryouzband, A.; Joonaki, E.; Edlmann, K.; Heinemann, N.; Yang, J.,
623 Thermodynamic and transport properties of hydrogen containing streams. *Sci Data* **2020,** *1*
624 (1), 1-14.
625 5. Heinemann, N.; Booth, M. G.; Haszeldine, R. S.; Wilkinson, M.; Scafidi, J.;
626 Edlmann, K., Hydrogen storage in porous geological formations - onshore play opportunities
627 in the Midland Valley (Scotland, UK). *Int J Hydrog Energy* **2018,** *43* (45), 20861-20874.
628 6. Thaysen, E. M.; McMahon, S.; Strobel, G. J.; Butler, I. B.; Ngwenya, B. T.;
629 Heinemann, N.; Wilkinson, M.; Hassanpouryouzband, A.; McDermott, C. I.; Edlmann, K.,
630 Estimating microbial growth and hydrogen consumption in hydrogen storage in porous media
631 *Renew Sustain Energ Rev* **2021,** *151* (111481), 1-15.
632 7. Matos, C. R.; Carneiro, J. F.; Silva, P. P., Overview of large-scale underground
633 energy storage technologies for integration of renewable energies and criteria for reservoir
634 identification. *J. Energy Storage* **2019,** *21*, 241-258.
635 8. Heinemann, N.; Alcalde, J.; Miocic, J.; Hangz, S. J. T.; Kallmeyer, J.; Ostertag-
636 Henning; Hassanpouryouzband, A.; Thaysen, E. M.; Strobel, G.; Wilkinson, M.; Schmidt-
637 Hattenberger, C.; Edlmann, K.; Bentham, M.; Haszeldine, S.; Carbonell, R.; Rudloff, A.,

638 Enabling large-scale hydrogen storage in porous media: the scinetific challenges. *Energy*
639 *Environ Sci* **2021,** *14*, 853-864.
640 9. Paterson, L., The implications of fingering in underground hydrogen storage. *Int J*
641 *Hydrogen Energ* **1983,** *8* (1), 53-59.
642 10. Chaturvedi, K. R.; Bajpai, S.; Trivedi, J.; Sharma, T., Air foams for mobility control
643 and subsurface storage of hydrogen in porous media: An experimental study. *Energy & Fuels*
644 **2022,** *36*, 5036-5046.
645 11. Flesch, S.; Pudlo, D.; Albrecht, D.; Jacob, A.; Enzmann, F., Hydrogen underground
646 storage-Petrographic and petrophysical variations in reservoir sandstones from laboratory
647 experiments under simulated reservoir conditions. *Int J Hydrog Energy* **2018,** *43* (45), 20822-
648 20835.
649 12. Yekta, A. E.; Pichavant, M.; Audigane, P., Evaluation of geochemical reactivity of
650 hydrogen in sandstone: Application to geological storage. *J Appl Geochem* **2018,** *95*, 182-
651 194.
652 13. Hassanpouryouzband, A.; Adie, K.; Cowen, T.; Thaysen, E. M.; Heinemann, N.;
653 Butler, I. B.; Wilkinson, M.; Edlmann, K., Geological Hydrogen Storage: Geochemical
654 Reactivity of Hydrogen with Sandstone Reservoirs. *ACS Energy Lett* **2022,** *7*, 2203-2210.
655 14. Yekta, A. E.; Manceau, J. C.; Gaboreau, S.; Pichavant, M.; Audigane, P.,
656 Determination of Hydrogen-Water Relative Permeability and Capillary Pressure in
657 Sandstone: Application to Underground Hydrogen Injection in Sedimentary Formations.
658 *Transport Porous Med* **2018,** *122* (2), 333-356.
659 15. Rezaei, A.; Hassanpouryouzband, A.; Molnar, I.; Derikvand, Z.; Haszeldine, R. S.;
660 Edlmann, K., Relative permeability of hydrogen and aqueous brines in sandstones and
661 carbonates at reservoir conditions. *Geophys Res Lett* **2022**.

16. Higgs, S.; Da Wang, Y.; Sun, C.; Ennis-King, J.; Jackson, S. J.; Armstrong, R. T.; Mostaghimi, P., In-situ hydrogen wettability characterisation for underground hydrogen storage. *Int J Hydrog Energy* **2021,** *47* (26), 13062-13075.

17. Esfandyari, H.; Sarmadivaleh, M.; Esmaeilzadeh, F.; Ali, M.; Iglauer, S.; Keshavarz, A., Experimental evaluation of rock mineralogy on hydrogen-wettability: Implications for hydrogen geo-storage. *J Energy Storage* **2022,** *52* (104866), 1-8.

18. Hashemi, L.; Glerum, W.; Farajzadeh, R.; Hajibeygi, H., Contact angle measurement for hydrogen/brine/sandstone system using captive-bubble method relevant for underground hydrogen storage. *Adv Water Resour* **2021,** *154* (103964), 1-13.

19. Iglauer, S.; Muhammad, A.; Keshavarz, A., Hydrogen wettability of sandstone reservoirs: implications for hydrogen geo-storage. *Geophys Res Lett* **2020,** *48* (3), 1-5.

20. Lysyy, M.; Ersland, G.; Fernø, M., Pore-scale dynamics for underground porous media hydrogen storage. *Adv Water Resour* **2022,** *163* (104167), 1-13.

21. Al-Yaseri, A.; Jha, N. K., On hydrogen wettability of basaltic rock. *J Pet Sci Eng* **2021,** *200*, 1-5.

22. Hosseini, M.; Ali, M.; Fahimpour, J.; Keshavarz, A.; Iglauer, S., Basalt-$H_2$-brine wettability at geo-storage conditions: Implication for hydrogen storage in basaltic formation. *J Energy Storage* **2022,** *52* (104745), 1-6.

23. van Rooijen, W.; Hashemi, L.; Boon, M.; Farajzadeh, R.; Hajibeygi, H., Microfluidics-based analysis of dynamic contact angles relevant for underground hydrogen storage. *Adv Water Resour* **2022,** *164* (104221), 1-17.

24. Al-Yaseri, A.; D., W.-B.; Fauziah, C. A.; Iglauer, S., Hydrogen wettability of clays: Implications for underground hydrogen storage. *Int J Hydrog Energy* **2021,** *46* (69), 34356-34361.

686 25. Azin, R.; Izadpanahi, A., *Fundamentals and practical aspects of gas injection*
687 Springer: 2022.
688 26. Morrow, N.; Chatzis, I.; Taber, J. J., Entrapment and mobilization of residual oil in
689 bead packs. *SPE Reservoir Engineering* **1988,** *3* (3).
690 27. Blunt, M. J.; Bijeljic, B.; Dong, H.; Gharbi, O.; Iglauer, S.; Mostaghimi, P.;
691 Paluszny, A.; Pentland, C. H., Pore-scale imaging and modelling. *Adv Water Resour* **2013,**
692 *51*, 197-216.
693 28. Saraf, S.; Bera, A., A review on pore-scale modeling and CT scan technique to
694 characterize the trapped carbon dioxide in impermeable reservoir rocks during sequestration.
695 *Renew Sust Energ Rev* **2021,** *144* (110986), 1-20.
696 29. Xu, L.; Myers, M.; Li, Q.; White, C.; Zhang, X., Migration and storage
697 characteristics of supercritical $CO_2$ in anisotropic sandstones with clay interlayers based on
698 micro-CT experiments. *J Hydrol* **2020,** *580* (124239), 1-17.
699 30. Iglauer, S.; Paluszny, A.; Pentland, C. H.; Blunt, M. J., Residual $CO_2$ imaged with x-
700 ray micro-tomography. *Geophys Res Lett* **2011,** *38* (L21403), 1-6.
701 31. Andrew, M.; Menke, H.; Blunt, M. J.; Bijeljic, B., The imaging of dynamic
702 multiphase fluid flow using synchrotron-based x-ray microtomography at reservoir
703 conditions. *Tranp Porous Med* **2015,** *110* (1), 1-24.
704 32. Andrew, M.; Bijeljic, B.; Blunt, M. J., Pore-scale imaging of trapped supercritical
705 carbon dioxide in sandstones and carbonates. *Int J Greenh Gas Control* **2014,** *22*, 1-14.
706 33. Krevor, S. C. M.; Pini, R.; Zuo, L.; Benson, S. M., Relative permeability and
707 trapping of $CO_2$ and water in sandstone rocks at reservoir conditions. *Water Resour Res* **2012,**
708 *48*, 1-16.
709 34. Rahman, T.; Lebedev, M.; Barifcani, A.; Iglauer, S., Residual trapping of
710 supercritical $CO_2$ in oil-wet sandstone. *J Colloid Interf Sci* **2016,** *469*, 63-68.

711 35. Niu, B.; Al-Menhali, A.; Krevor, S. C., The impact of reservoir conditions on the
712 residual trapping of carbon dioxide in Berea sandstone. *Water Resour Res* **2015,** *51* (4), 2009-
713 2029.
714 36. Cao, Q.; Gong, Y.; Fan, T.; Wu, J., Pore-scale simulations of gas storage in tight
715 sandstone reservoirs for a sequence of increasing injection pressure based on micro-CT. *J Nat*
716 *Gas Sci Eng* **2019,** *64*, 15-27.
717 37. Khishvand, M.; Alizadeh, A. H.; Piri, M., In-situ characterization of wettability and
718 pore-scale displacements during two- and three-phase flow in natural porous media. *Adv*
719 *Water Resour* **2016,** *97*, 270-298.
720 38. Sarmadivaleh, M.; Al-Yaseri, A.; Iglauer, S., Influence of temperature and pressure
721 on quartz–water–$CO_2$ contact angle and $CO_2$–water interfacial tension. *J Colloid Interf Sci*
722 **2015,** *441*, 59-64.
723 39. Al-Yaseri, A.; Esteban, L.; Giwelli, A.; Sarout, J.; Lebedev, M.; Sarmadivaleh, M.,
724 Initial and residual trapping of hydrogen and nitrogen in Fontainebleau sandstone using
725 nuclear magnetic resonance core flooding. *Int J Hydrog Energy* **2022,** *in press*.
726 40. Jha, N. K.; Al-Yaseri, A.; Ghasemi, M.; Al-Bayati, D.; Lebedev, M.; Sarmadivaleh,
727 M., Pore scale investigation of hydrogen injection in sandstone via X-ray micro-tomography.
728 *Int J Hydrog Energy* **2021,** *46*, 34822-34829.
729 41. Pak, T.; Butler, I. B.; Geiger, S.; van Dijke, M. I. J.; Sorbie, K. S., Droplet
730 fragmentation: 3D imaging of a previously unidentified pore-scale process during multiphase
731 flow in porous media. *P Natl Acad Sci USA* **2015,** *112* (7), 1947-1952.
732 42. Iglauer, S.; Ferno, M. A.; Shearing, P.; Blunt, M. J., Comparison of residual oil
733 cluster size distribution, morphology and saturation in oil-wet and water-wet sandstone. *J*
734 *Colloid Interf Sci* **2012,** *375*, 187-192.

43. Iglauer, S.; Paluszny, A.; Blunt, M. J., Simultaneous oil recovery and residual gas storage: A pore-level analysis using in situ X-ray micro-tomography. *Fuel* **2013,** *103*, 905-914.

44. Pentland, C. H.; Tanino, Y.; Iglauer, S.; Blunt, M. J., Capillary trapping in water-wet sandstones: coreflooding experiments and pore-network modeling. In *SPE International* Society of Petroleum Engineers Florence, Italy 2010.

45. Fusseis, F.; Steeb, H.; Xiao, X.; Zhu, W.-l.; Butler, I. B.; Elphick, S.; Maeder, U., A low-cost X-ray-transparent experimental cell for synchrotron-based X-ray microtomography studies under geological reservoir condition. *J Synchrotron Radiation* **2014** *21* (1), 251-253.

46. Pak, T. Saturation tracking and identification of residual oil saturation. University of Edinburgh 2014.

47. Kumar, M.; Sok, R.; Knackstedt, M. A.; Latham, S.; Senden, T. J.; Sheppard, A. P.; Varslot, T.; Arns, C. In *Mapping fluid distributions in 3D at the pore scale: Quantifying the influence of wettability and saturation*

*history on rock resistivity*, SPWLA 50th Annual Logging Symposium, Society of Petrophysicists and Well-Log Analysts: 2009.

48. Yusibani, E.; Nagahama, Y.; Kohno, M.; Takata, Y.; Woodfield, P. L.; Shinzato, K.; Fujii, M., A capillary tube viscometer designed for measurements of hydrogen gas viscosity at high pressure and high temperature. *Int J Thermophys* **2011,** *32* (6), 1111-1124.

49. Chow, Y. T. F.; Maitland, G. C.; Trusler, J. P. M., Interfacial tensions of (H2O + H-2) and (H2O + CO2 + H-2) systems at temperatures of (298-448) K and pressures up to 45 MPa. *Fluid Phase Equilibr* **2018,** *475*, 37-44.

50. Chow, Y. T. F.; Maitland, G. C.; Trusler, J. P. M., Erratum to "Interfacial tensions of (H2O + H-2) and (H2O + CO2 + H-2) systems at temperatures of (298-448) K and pressures up to 45 MPa". *Fluid Phase Equilibr* **2020,** *503* (112315), 1.

51. Nakai, T.; Sawamura, S.; Taniguchi, Y.; Yamaura, Y., Effect of pressure on the viscosity B coefficient of cesium chloride in water *Mater Sci Res Int* **1996,** *2* (3), 143-147.

52. Vlassenbroeck, J.; Masschaele, B.; Cnuddle, V.; Dierick, M.; Pieters, K.; Van Hoorebeke, L.; Jacobs, P., Octopus 8: A high performance tomographic reconstruction package for X-ray tube and synchrotron micro-CT. In *Advances in X-ray tomography for geomaterials*, Desrues, J.; Viggiani, G.; Bésuelle, P., Eds. ISTE: London, UK, 2010.

53. Buades, A.; Coll, B.; Morel, J. M. In *A non-local algorithm for image denoising*, 2005 IEEE Computer Society Conference on Computer Vision and Pattern Recognition (CVPR'05), 2005; pp 60-65.

54. Blunt, M. J., *Multiphase flow in permeable media. A Pore-scale perspective* Cambridge University Press Cambridge, United Kingdom, 2017.

55. Singh, K.; Menke, H.; Andrew, M.; Lin, Q.; Rau, C.; Blunt, M. J.; Bijeljic, B., Dynamics of snap-off and porefilling events during two-phase fluid flow in permeable media. *Sci Rep* **2017,** *7* (5192), 1-13.

56. Roof, J. G., Snap-off of oil droplets in water-wet pores. *Soc Petrol Eng J* **1970,** *10* (1), 85-90.

57. Thomas, L. K.; Katz, D. L.; Tek, M. R., Threshold pressure phenomena in porous media. *Soc Petrol Eng J* **1968**, 174-184.

58. Boone, M. A.; Kock, T. D.; Bultreys, T.; Schutter, G. D.; Vontobel, P.; Hoorebeke, L. V.; Cnudde, V., 3D mapping of water in oolithic limestone at atmospheric and vacuum saturation using X-ray micro-CT differential imaging. *Mater Char* **2014,** *97*, 150-160.

59. De Lucia, M.; Pilz, P.; Liebscher, A.; Kuhn, M., Measurements of H2 solubility in saline solutions under reservoir conditions: preliminary results from project H2STORE. *Enrgy Proced* **2015,** *76*, 487-494.

60. Herring, A. L.; Harper, E.; Andersson, L.; Sheppard, A.; Bay, B. K.; Wildenschild, D., Effect of fluid topology on residual nonwetting phase trapping: Implications for geologic $CO_2$ sequestration. *Adv Water Resour* **2013,** *62*, 47-58.

61. Hassanpouryouzband, A.; Joonaki, E.; Edlmann, K.; Haszeldine, R. S., Offshore Geological Storage of Hydrogen: Is This Our Best Option to Achieve Net-Zero? *ACS Energy Lett* **2021,** *6* (6), 2181–2186.

62. Wagner, O. R.; Leach, R. O., Effect of interfacial tension on displacement efficiency. *SPE J* **1966,** *6* (4), 335-344.

63. Avraam, D. G.; Payatakes, A. C., Flow Mechanisms, Relative Permeabilities, and Coupling Effects in Steady-State Two-Phase Flow through Porous Media. The Case of Strong Wettability. *Ind Eng Chem Res* **1999,** *38*, 778-786.

64. Cho, J.; Kim, T. H.; Chang, N.; Lee, K. S., Effects of relative permeability change resulting from interfacial tension reduction on vertical sweep efficiency during the CO2-LPG hybrid EOR process. *Energy Sources* **2018,** *40* (10), 1242-1249.

65. Sabet, N.; Hassanzadeh, H.; Abedi, J., Stability of Gravitationally Unstable Double Diffusive Transient Boundary Layers with Variable Viscosity in Porous Media. *Aiche J* **2017,** *63* (6), 2471-2482.

66. Oughanem, R.; Youssef, S.; Peysson, Y.; Bazin, B.; Maire, E.; Vizika, O., Pore-scale to core-scale study of capillay desaturation curves ulti multi-scale 3D imaging In *International Symposium of the Society of Core Analysts*, Napa Valley, California, USA, 2013.

806 67. Ding, M.; Kantzas, A., Capillary number correlations for gas-liquid systems. *J Can*
807 *Petrol Technol* **2007,** *46* (27-32).

808

809

# Supplementary Information

# Pore-scale imaging of hydrogen displacement and trapping in porous media

Eike M. Thaysen[2*], Ian Butler[1], Damien Freitas[1], Aliakbar Hassanpouryouzband[1], Fernando Alvarez-Borges[2], Samuel C. Krevor[3], Niklas Heinemann[1], Robert Atwood[2], Katriona Edlmann[1]

[1]School of Geoscience, Grant Institute, The King's Buildings, The University of Edinburgh, James Hutton Road, Edinburgh, EH9 3FE, United Kingdom

[2] Diamond Light Source Ltd, Harwell Campus, Didcot OX11 0DE, UK

[3] Department of Earth Science and Engineering, Imperial College London, London SW7 2AZ, United Kingdom

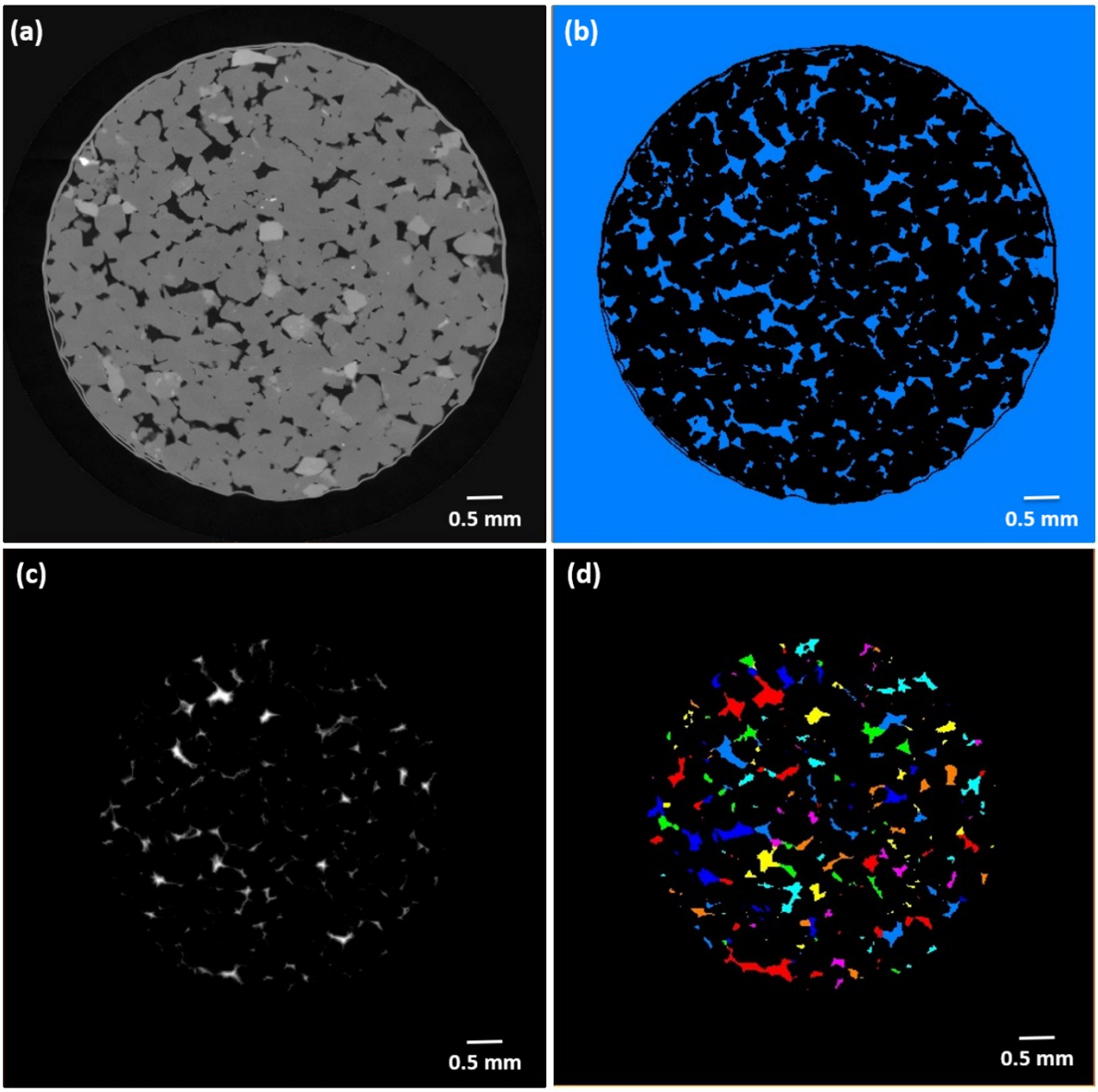


SI Figure S1: Image processing workflow for UoE experiments. **(a)** The image after reconstruction and filtering. **(b)** The image after segmenting using a global threshold. **(c)** The outer part of the rock core touching the Al foil was removed through application of a mask, and a chamfer distance map of the pore space was calculated by assigning each voxel the distance from it to the nearest pore wall. **(d)** This was then used to separate the pore space into individual pores by calculating the water-shed basins of the distance map.

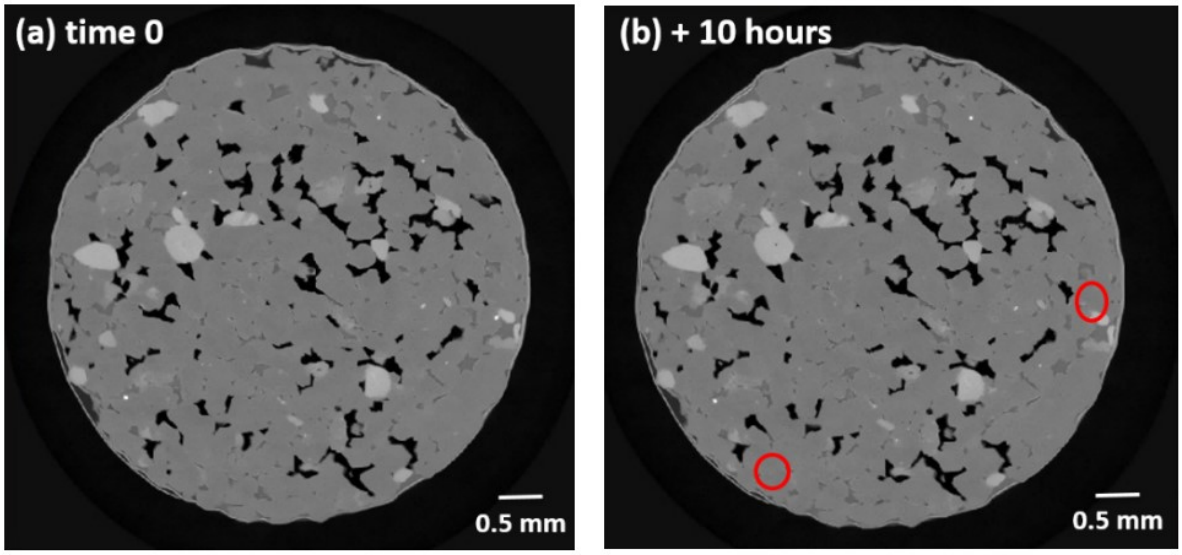


SI Figure S2: $H_2$ stability at 7 MPa injection pressure and a flow rate of 20 µl $min^{-1}$ (capillary number $2*10^{-8}$) at time zero **(a)** and after ten hours **(b)**. Red circles indicate subtle differences in the hydrogen filled pore volume after ten hours. The difference in the hydrogen saturation for the total scanned rock volume was within error at 49.55% % and 49.53% for time 0 and after ten hours, respectively.

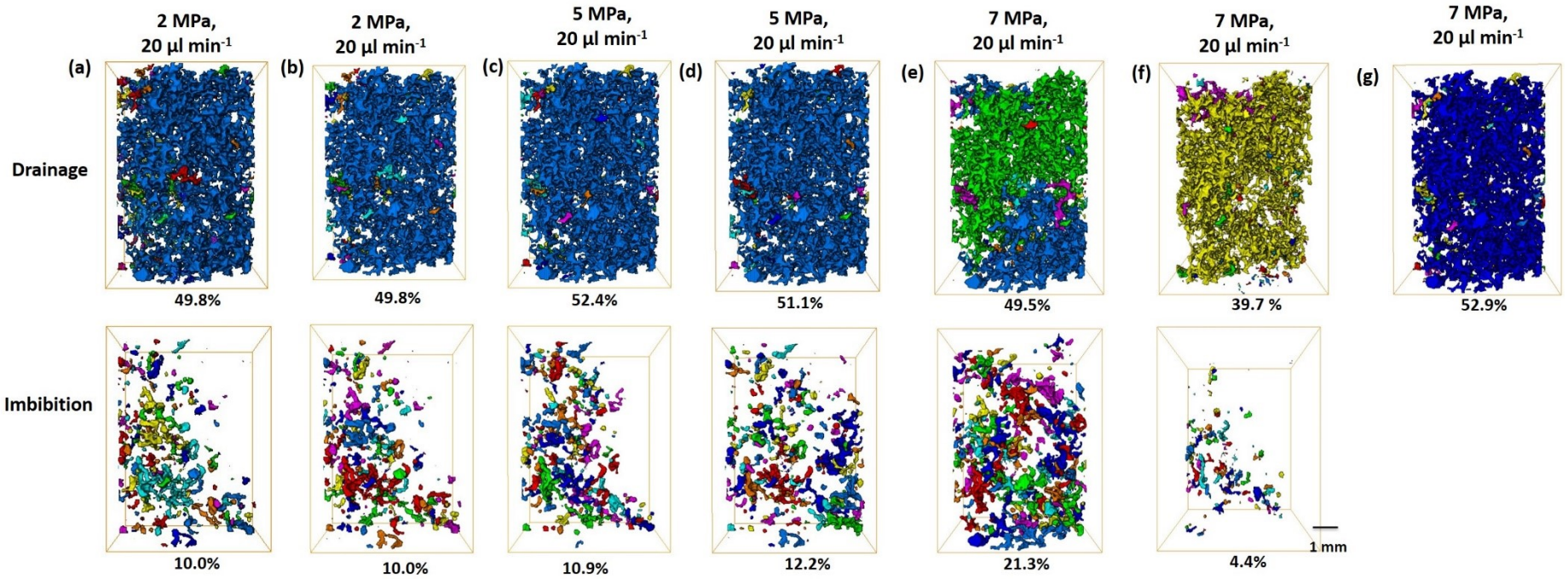


SI Figure S3: Enlarged view of 3D renderings of $H_2$ with saturation percentages in UoE experiments. Discrete clusters were rendered in colours, where mainly one colour marks one large, connected cluster and different colours indicate several, not connected clusters. **(a-d)** Effect of pore fluid pressure on $H_2$ clusters and saturation after drainage and after primary imbibition. **(a)** 2 MPa, **(b)** 5 MPa and **(c-e)** 7 MPa, all at a constant flow rate of 20 µl $min^{-1}$ corresponding to capillary numbers of $1.7x10^{-8}$ and $2.4x10^{-6}$, respectively.. Experiments were repeated once. For experiments at 2 MPa and 5 MPa averages and standard errors for the $H_2$ saturation are reported. For experiments at 7 MPa, due to the discrepancy in the results, both results are visualized **(c-d)**.

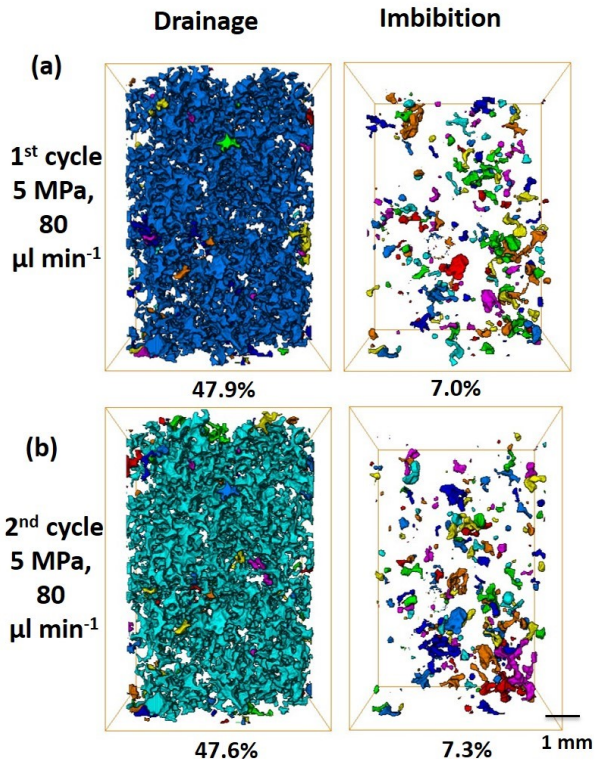


SI Figure S4: Cyclic $H_2$ injection into Clashach sandstone at 5 MPa and 80 µl $min^{-1}$ corresponding to a capillary number of $9.4x10^{-6}$, showing no significant differences in $H_2$ saturation and $H_2$ connectivity after primary drainage and imbibition as compared to after secondary drainage and imbibition.

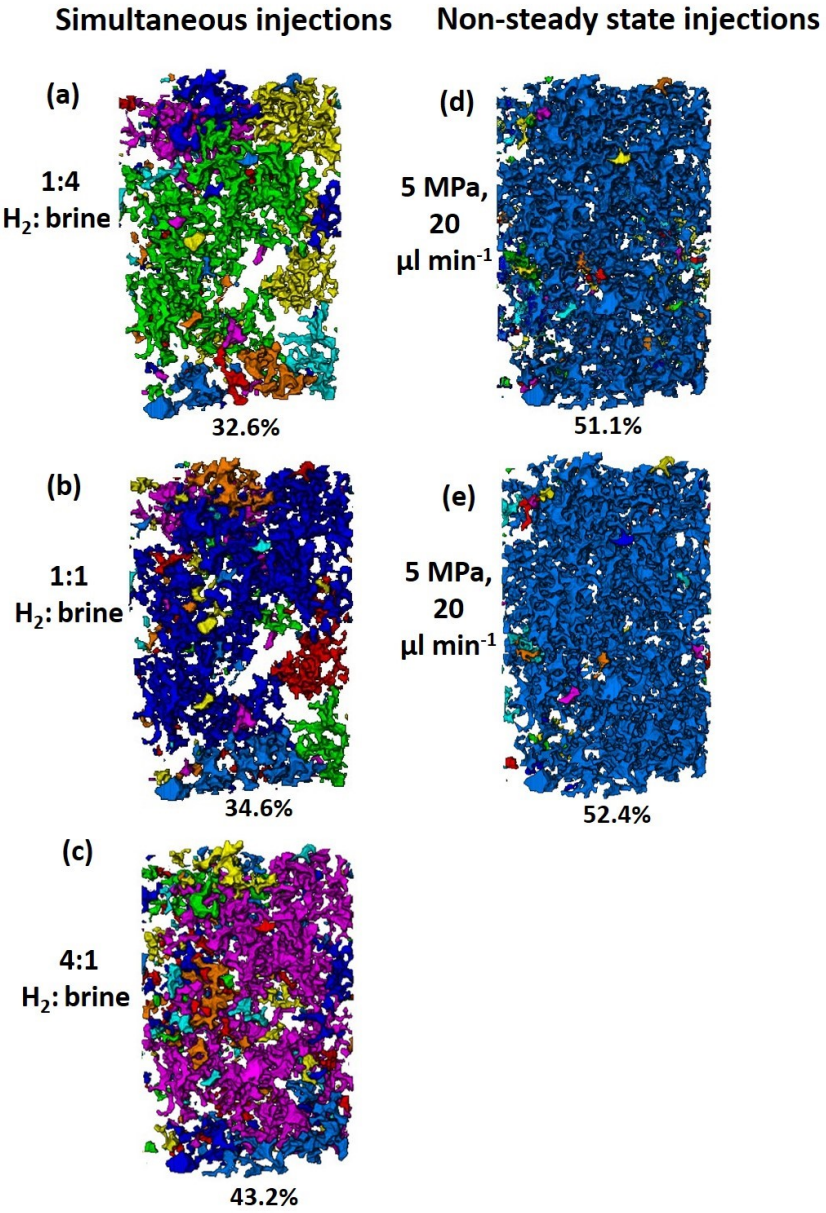


SI Figure S5: Comparison of the distribution of the $H_2$ clusters in the pore space between simultaneous $H_2$ and brine injection experiments **(a-c)** and the two repetitions of the non-steady state $H_2$ injection **(d)** and **(e)**, all at 5 MPa and a total flow rate of 20 µl $min^{-1}$.

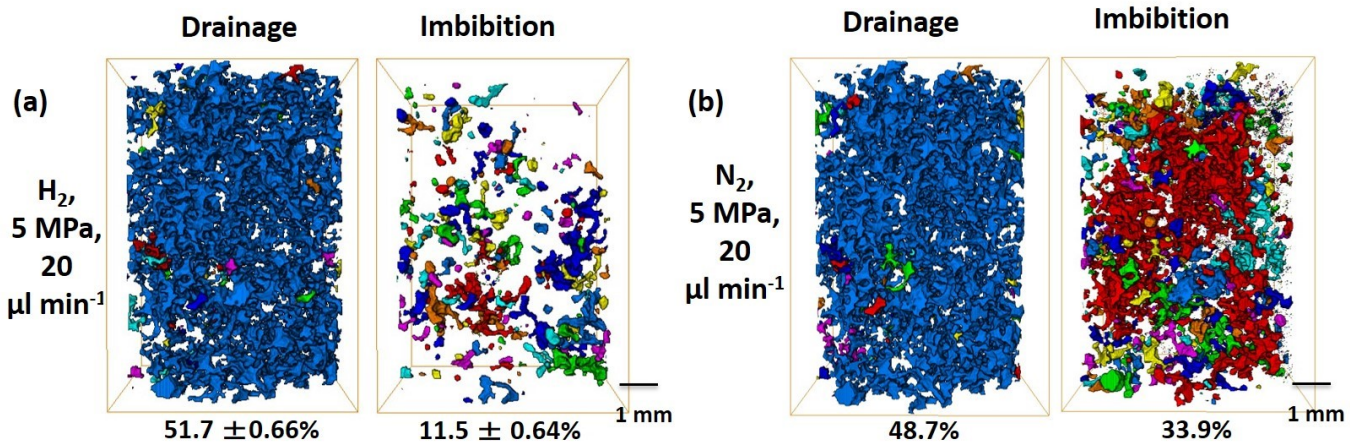


SI Figure S6: Nitrogen clusters and saturations during drainage and imbibition at 5 MPa pore fluid pressure and a flowrate of 20 µl $min^{-1}$